Geometrically Enhanced Thermoelectric Effects in Graphene Nanoconstrictions

Achim Harzheim,[†,//] Jean Spiece,[‡,//] Charalambos Evangeli,[†,‡] Edward McCann,[‡] Vladimir Falko,[§] Yuewen Sheng,[†] Jamie H. Warner,[†] G. Andrew D. Briggs,[†] Jan A. Mol,[†] Pascal Gehring, [†,¶,] and Oleg V. Kolosov,[‡,*]*

[†] Department of Materials
University of Oxford
Parks Road, OX1 3PH Oxford, UK

[‡] Department of Physics
Lancaster University
Bailrigg, LA1 4YB, Lancaster, UK

[§] School of Physics & Astronomy
University of Manchester
Oxford Road, M13 9PL, Manchester, UK

[¶] Kavli Institute of Nanoscience
Delft University of Technology
Lorentzweg 1, 2628 CJ, Delft, Netherlands

KEYWORDS: thermoelectrics, Peltier, Seebeck, graphene nanostructures, scanning thermal microscopy

ABSTRACT. The influence of nanostructuring and quantum confinement on the thermoelectric properties of materials has been extensively studied. While this has made possible multiple breakthroughs in the achievable figure of merit, classical confinement and its effect on the local Seebeck coefficient has mostly been neglected, as has the Peltier effect in general due to the complexity of measuring small temperature gradients locally.

Here we report that reducing the width of a graphene channel to 100 nanometers changes the Seebeck coefficient by orders of magnitude. Using a scanning thermal microscope allows us to probe the local temperature of electrically contacted graphene two-terminal devices or to locally heat the sample. We show that constrictions in mono- and bilayer graphene facilitate a spatially correlated gradient in the Seebeck and Peltier coefficient, as evidenced by the pronounced thermovoltage V_{th} and heating/cooling response $\Delta T_{\mathrm{Peltier}}$ respectively. This geometry dependent effect, which has not been reported previously in 2D materials, has important implications for measurements of patterned nanostructures in graphene and points to novel solutions for effective thermal management in electronic graphene devices or concepts for single material thermocouples.

TEXT. Solid-state thermoelectric devices have long been attractive to researchers and engineers alike, due to their capability of reliably converting waste heat to electricity and the possible thermal management applications.[1–4] In addition, an in-depth understanding of thermoelectric phenomena is important to correctly interpret photocurrent and electrical transport measurements where these

phenomena can play a major role.[4,5] There are two complementary thermoelectric effects, the Seebeck effect and its Onsager reciprocal, the Peltier effect. For the first, a temperature difference ΔT will induce the buildup of a thermovoltage $\Delta V = -S\Delta T$ across a material with a Seebeck coefficient *S*. Vice versa, for the second, an electrical current I induces a heat flow $\dot{Q} = \Pi I$, where $\Pi = TS$ is the Peltier coefficient.[6]

A resurge in interest in this topic was initiated by Hicks and Dresselhaus' theoretical findings that reducing the dimensionality of thermoelectric materials could significantly increase their efficiency.[7,8] This is measured by the dimensionless figure of merit $ZT = \frac{S^2\sigma}{\kappa}T$ – a function of the electrical (σ) and thermal (κ) conductivity – and the principle has since been demonstrated by various groups.[9,10] Amongst the techniques that have been employed are building nanocomposites from nanocrystal blocks,[11] nanostructuring quantum dot superlattices,[9] the exploitation of negative correlations between electrical and thermal conductivity,[12] and band engineering.[13,14] Moreover, classical rather than quantum confinement has been reported to cause an increase in the Seebeck coefficient in gold and Antimony Telluride nanowires.[15,16]

Here we present high resolution Scanning Thermal Microscopy measurements of 100 nm wide graphene bow-tie nanoconstrictions that show a pronounced spatial dependence of the Seebeck and the Peltier effect. This change in the local Seebeck coefficient is attributed to a shortened effective Electron Mean Free Path (EMFP) due to edge scattering and opens up the possibility to readily produce two dimensional one-material thermocouples as well as accessible local temperature management and improved heat dissipation.

We perform our measurements with a Scanning Thermal Microscope (SThM) – effectively an atomic force microscop (AFM) with a microfabricated resistor incorporated in the tip[17] - using two

different protocols to map the Seebeck and Peltier effect as well as the Joule heating. In the Peltier measurement, we use a recently developed non-equilibrium scanning probe thermometry method:[18] an AC bias V_{bias} applied to the device through the global contacts causes an AC current I_{bias} which results in Joule heating and Peltier heating/cooling. By measuring the temperature response of our SThM tip as it is scanned over the AC biased sample and modulating it at the first (Peltier) and second (Joule) harmonic it is possible to decouple the two effects and extract the respective heating/cooling values (see Figure 1a for the measurement schematics). In contrast, for the thermovoltage or Seebeck measurement, the SThM tip is heated by applying a high AC voltage to it and the global voltage drop over the device is recorded at the second harmonic as the hot tip is scanned over the sample. Both single layer and multilayer graphene are measured, but no thickness dependence in the size and distribution of the signal is found.

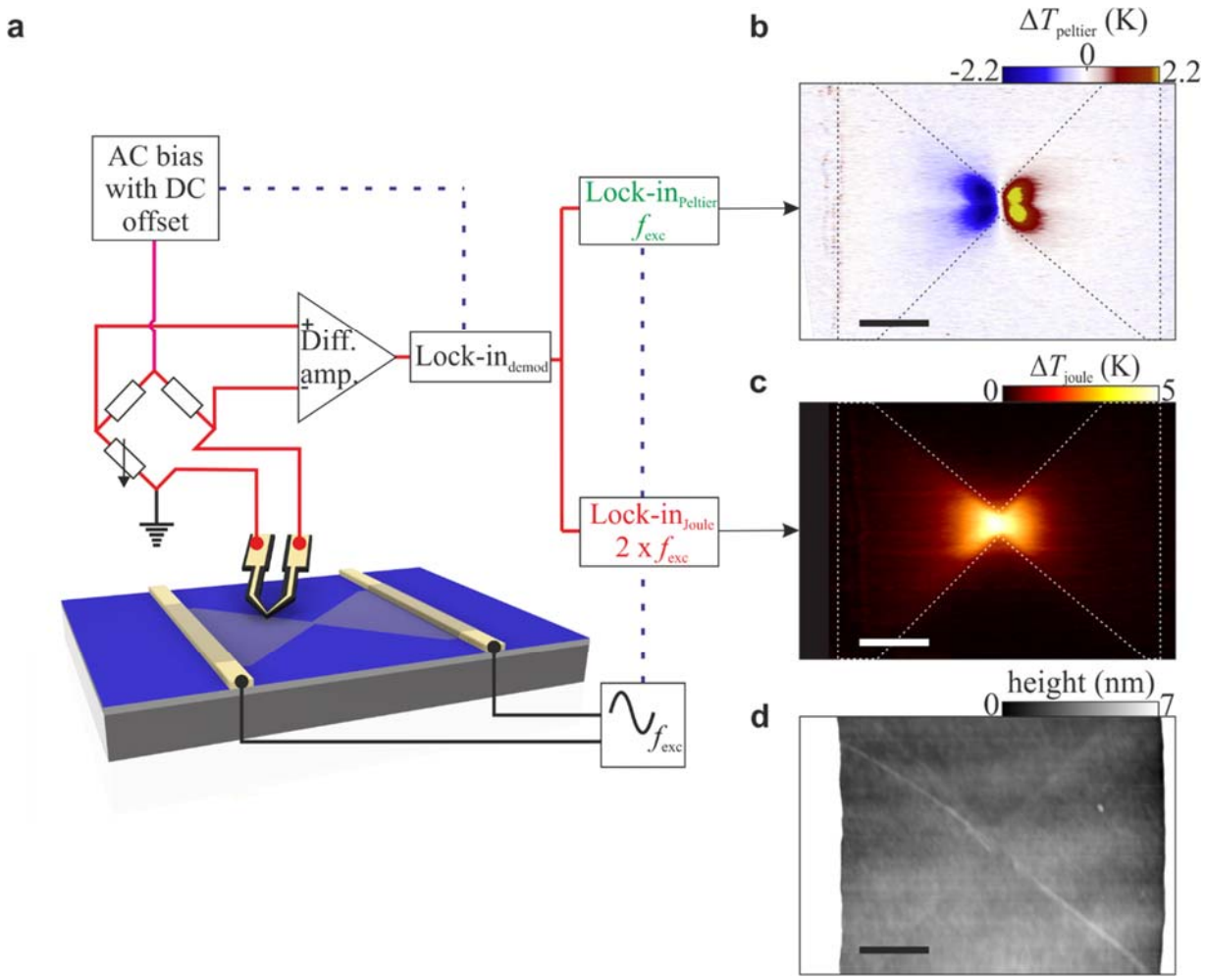

Figure 1. Nanoscale mapping of the Peltier effect in graphene nanoconstrictions. (a) An AC voltage bias V_{bias} at f_{exc} induces an AC current I_{bias} through the constriction (black lines). In addition, a low AC bias with a DC offset is applied to the SThM tip through a Wheatstone bridge (magenta line). During scanning, the resulting signal in the tip (red lines) is demodulated at the respective frequency. This thermal signal is then demodulated at the first (f_{exc}) and second ($2f_{\mathrm{exc}}$) harmonic, providing the Peltier heating/cooling (green) in b and Joule heating (red) in c, respectively. The blue dashed lines symbolize the reference signal lines. (b) Peltier effect map showing the main heating/cooling effects around the constriction (c) Joule heating map, showing the hot spot in the middle of the constriction. (d) Simultaneously recorded height map used to outline the position of the constriction in the Peltier heating/cooling and Joule heating images. In b and c, the dotted-dashed lines indicate the contact position and the dashed line the outline of the graphene constriction. All scale bars are 1 µm.

Peltier and Joule heating maps of the bow tie device, are shown in Figure 1b and c, respectively, where both show a high spatial dependence, with a strong signal around the constriction. The Joule heating exhibits a temperature increase while the Peltier signal shows cooling/heating on the respective side of the constriction and a node in the middle. The Peltier signal shown here importantly corresponds to the measured amplitude multiplied by the sine of the phase signal. It is the temperature at a certain phase at the maximum applied modulation voltage, since in time average no discernible Peltier heating or cooling is taking place at the constriction for an AC bias.[18] Figure 1d shows the simultaneously measured height signal, which was used to determine the exact position of the device indicated in b and c.

The Joule heating showing a maximum in the constriction is expected due to the increased local current density,[19] however, given the continuous composition of the material in the constriction area, all thermoelectric effects in the device would be expected only in the vicinity of the Au electrodes.[20] As can be seen in Figure 1b, the Peltier signal $\Delta T_{\mathrm{Peltier}}$ becomes strongest around the constriction itself and outlines the shape of the graphene bow-tie where the signal at the edges is broadened out due to heat spreading into the surrounding SiO_2 substrate. The SThM measurement of the device without current excitation, also observed by Tovee et al,[21] show that the heat dissipation from the heated tip in the areas with and without graphene differs by less than 5% (see SI section 7). These suggest that it is reasonable to assume that SiO_2/Si substrate plays dominant role in the heat spreading. The Peltier effect results in heating and cooling of up to $\Delta T_{\mathrm{Peltier}} \approx \pm 2\mathrm{K}$ on either side of the constriction for an applied current of $I_{bias} \approx 90\mu\mathrm{A}$. A markedly similar behavior was found for V_{th} in the thermovoltage measurements on the same device (see Figure S5 in the Supporting Information) under open-circuit condition, confirming that the signal likely stems from a changed local Seebeck coefficient. In addition, we observe comparatively weak "conventional"

Peltier heating/cooling in the vicinity of the Au contacts (see Figure 1b) which is explained by the formation of a Peltier junction between gold and graphene at the contacts as reported previously.[4,20]

Such a geometrical modification of the local Seebeck coefficient has been seen in metallic thin-film stripes and Au nanowires and was explained by structural defects and the metal grain structure, which in turn reduce the EMFP.[15,22] The EMFP of graphene at room temperature, is typically on the order of 100s of nanometers and thus higher than in gold.[23] However, it gets substantially reduced by defect potentials such as ones stemming from rough edges,[24] which in our case have been created by the device patterning and amount up to an 80% reduction.[25] This edge scattering becomes more dominant as the width of the graphene stripe $\Delta y(x)$ reduces, giving a position dependent mean free path, which can be written as

$$l(x) = l_0 \left[1 + c_n \left(\frac{l_0}{\Delta y(x)}\right)^n\right]^{-1}, \quad (1)$$

where l_0 is the bulk mean free path and c_n and n are numerical coefficients specifying the transport mode and the influence of scattering on the mean free path (see section 11 in the Supporting Information). To extract the bulk mean free path we perform gate conductance measurements on 43 µm long and 3 µm wide graphene ribbons that give us $l_0 \approx 226 \pm 20$ nm (see section 3 Supporting Information).

Using the Mott formula $S = \frac{\pi^2 k_B^2 T}{3e} \frac{1}{R(\epsilon)} \frac{dR(\epsilon)}{d\epsilon}\Big|_{\epsilon=\epsilon_F}$ we obtain an expression for the thermopower as a function of constriction width (see section 11 in the Supporting Information for more information):

$$S = -\frac{\pi^2 k_B^2 T}{3\epsilon_F e}\left[1 + n\, U \frac{l(x)}{l_0} - (n-1)U\right], \quad (2)$$

where $U = \frac{d \ln l_0}{d \ln \epsilon}\Big|_{(\epsilon=\epsilon_F)}$ is the exponent of any power law dependence of the EMFP on energy. We expect this value to be between the short range disorder or electron-phonon interaction value $U = -1$ and the long range Coulomb interaction $U = +1$.[26,27] Equation (2) predicts that the local Seebeck coefficient decreases when the width of the channel is reduced, which leads to regions with different effective Seebeck coefficients in the bow-tie shaped devices.

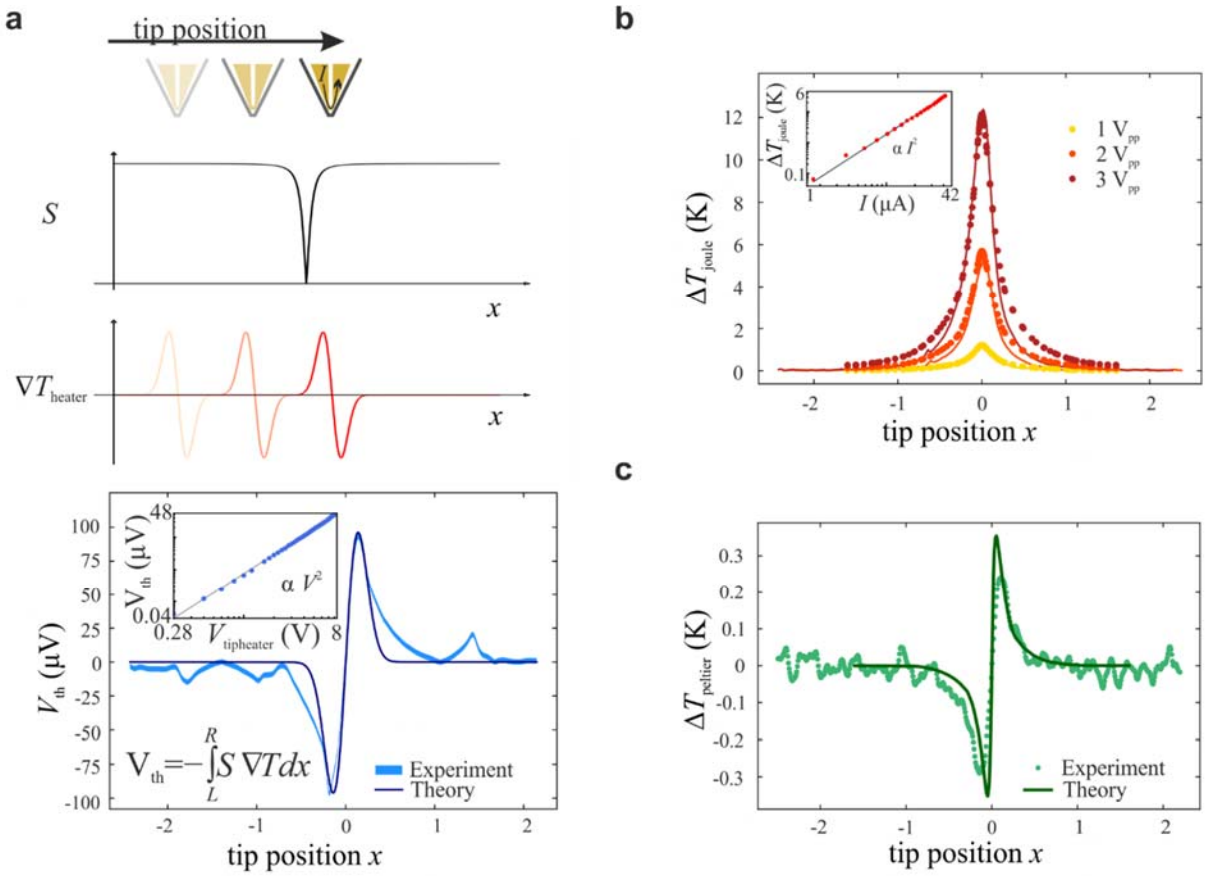

Figure 2. Modelling and fitting of Joule heating and thermoelectric effects in a bow-tie device. (a) From the top: schematic of the tip movement, 1D section cuts through the middle of the constriction of the calculated Seebeck coefficient, the tip-defined moving thermal gradient and the resulting thermovoltage measured and calculated respectively. The inset shows the quadratic tip voltage dependence of the thermovoltage signal in a log-log plot. (b) Joule heating at different applied voltage biases experimentally recorded (dots) and fitted to a COMSOL model (lines). The smallest Joule heating signal (1 V_{pp}, yellow) is used to extract the electrical and thermal conductivities for the entire model ($\kappa = 120\,\mathrm{Wm^{-1}K^{-1}}$, $\sigma = 5 \cdot 10^5\,\mathrm{Sm^{-1}}$). (c) Peltier heating/cooling at 1 V_{pp}, experimental and simulated from the COMSOL model using the calculated Seebeck coefficient from (a). The zero of the tip position is centered at the middle of the constriction for all figures.

Using Equation (1) and (2), we can model $V_{\mathrm{th}}(x)$ and compare it to the measured thermovoltage 1-D line section signals. As shown in Figure 2a, $V_{\mathrm{th}}(x) = -\int_L^R S\nabla T\, dx$ is calculated by taking the integral

of $S\nabla T$ over the whole length of the device at each point. In the measurement and in our calculations, the Seebeck coefficient is only dependent on the width of the constriction and its distribution does not change as we move the tip, while the temperature gradient ΔT_{tip} induced by the heater voltage V_{heater} is always centered at the tip position *x* and thereby moves as we scan over the sample. The heater temperature ΔT_{tip} is obtained from calibrating the tip and measuring the thermal resistance between the heater and the sample (see Supporting Information 7). It is worth noting here that there is an inherent uncertainty of the heater temperature that can lead to an over or underestimation of the measured effect, however this does not change the conclusion and main results of our work. Fitting the calculated values to the line cut of the thermovoltage measured with and estimated $\Delta T_{\mathrm{tip}} \approx 18 \pm 2$ K gives the dimensionless parameters $c_n \approx 0.56$, $n \approx 2.6$ and $U \approx 0.88$. Using these fitting values we calculate a bulk Seebeck coefficient of $S \approx 118$ µV K^{-1}, which is similar to previous measurements in graphene at room temperature.[28] The Seebeck coefficient in our model reduces from the bulk value of $S \approx 118\ \mu V K^{-1}$ to $S_{\mathrm{min}} \approx 0.34\ \mu V K^{-1}$ due to the reduction of the mean free path within the constriction. This orders of magnitude decrease is due to Equation (2) involving a difference of terms, resulting in a dramatically varying S for relatively small changes in the EMFP.

To further test the influence of geometrical confinement on the thermoelectric properties of graphene devices we have tested an "island" structure, where wide and narrow parts of graphene alternate and which is showing a pronounced signal at these junctions (see Figure S13 in the Supporting Information). It is worth to mention that applying a back gate voltage enables us to change the doping from p^{++}-doping (-30V) to p-doping (30V) which results in a modification of the signal strength in the constriction by approximately 20% due to the changed carrier density (see Figure S11 in the Supporting Information).[28]

The spatially dependent Seebeck coefficient extracted from the thermovoltage fit can be used to develop a COMSOL model that can reproduce our experimental Joule heating and Peltier signal (see Figure 2b and c). In this model the effective thermal conductivity $\kappa = 120\ \mathrm{W(mK)^{-1}}$ and the electrical conductivity $\sigma = 5 \cdot 10^5\ \mathrm{Sm^{-1}}$ are the only fit parameters with the spatial heat distribution determined mainly by the SiO_2 layer and only slightly modified by the fitted value of the thermal conductivity of a single graphene layer.

We have in addition studied the current dependence of all measured signals by placing the tip on one side of the constriction as the current through the device, I_{bias}, (in the Peltier and Joule heating measurements) or through the tip, I_{heater}, (in the thermovoltage measurements) is increased. In both the Joule heating and the thermovoltage measurements, a square current dependence on the current is observed (see Figure 2a and b inset), in agreement with the Joule-Lenz law ($P \propto I^2 R$).

However, in the Peltier measurement of the bow-tie device, we find that an initially linear dependence changes to a cubic one as we increase the current I_{bias}. As can be seen in Figure 3a, the data can be fitted with a combination of a cubic and linear term, where the crossover point is located at approximately $I_{\mathrm{bias}} = 33\ \mu\mathrm{A}$. This is a deviation from the simple linear dependence predicted by $\dot{Q} = \Pi * I_{bias} = ST * I_{\mathrm{bias}}$. We find this behavior in all geometries measured, with the crossover happening at different current levels (Figure S7 in the Supporting Information).

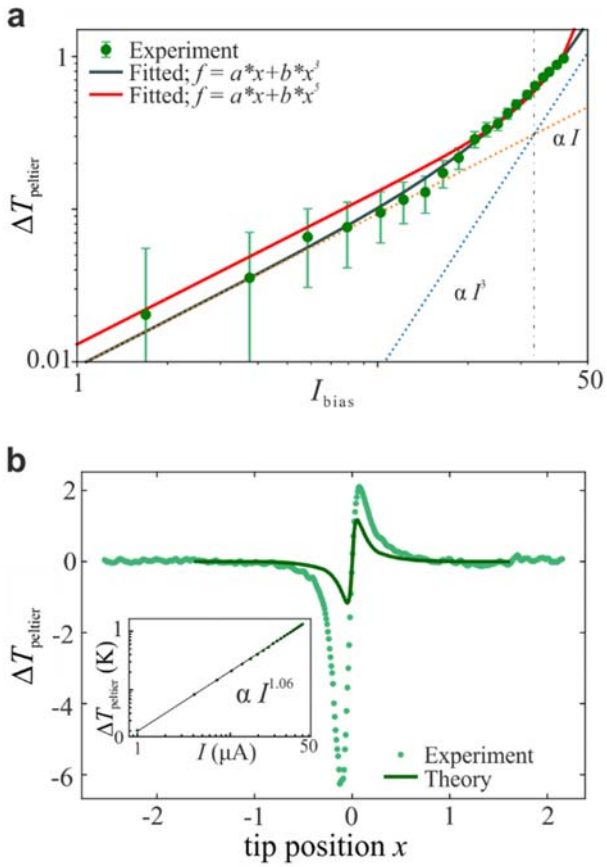

Figure 3. Deviation of the experimental data from the linear Peltier model. (a) Fit of the current dependency of the Peltier heating in the constriction for a linear and cubic (grey line) and fifth order term (red line). For the cubic dependency, which seems to fit the data better, the Peltier heating switches over from a linear to a cubic current dependency where the switchover point is marked by the black dotted-dashed line. The orange dotted line is linear with respect to the current and the blue dotted line is cubic and serve as a guide to the eye. (b) Comparison of the Peltier heating/cooling to the COMSOL model at $3V_{pp}$. A big discrepancy between the COMSOL model and the experimental data is visible both in shape and in amplitude. The asymmetry in the experimental data might be linked with the nanoscale asymmetry of the nanoconstriction. The inset shows the current dependency of the simulated Peltier heating, which is linear, save for a small correction ($\propto 1.02$) due to the Joule heating.

We attribute the unusual current dependence observed in our experiments to an "electron wind" effect: if the drift velocity v_{drift} becomes comparable to the Fermi velocity v_{F} heat is shifted with respect to the position of the constriction, effectively cooling one side and heating the other side. For this effect, we expect the Peltier heating/cooling to take the form of a sum of the common

linear Peltier effect and a cubic term. Here, in addition to the expected linear Peltier term, there is a contribution from an increasing drift velocity (linearly increasing with current) and the temperature of the hot carriers created by Joule heating (quadratic current dependency) that adds up to an additional cubic term. Indeed, we find that a fit of this model to the measured data provides a good agreement, compared to other higher order terms (see Figure 3 and SI). The drift velocity in our devices which is given by $v_{\mathrm{drift}} = \frac{I}{neW} \approx 0.25 \cdot 10^6 \mathrm{ms}^{-1}$ with $I \approx 40$ µA the current through the device, n the carrier density, e the elementary charge and $W = 100$ nm the width of the constriction is approaching the Fermi velocity in graphene, $v_{\mathrm{F}} \approx 10^6\ \mathrm{ms}^{-1}$. As we do not observe any significant electrical nonlinearity in the *I-V* traces, the carrier density is well approximated by the low current value of $n = 10^{16}\ \mathrm{m}^{-2}$. A similar electron wind effect has been observed for varying gate voltages in graphene devices.[29]

Another source for this discrepancy, the temperature dependence of the Seebeck coefficient and its increase caused by Joule heating would give a fifth order dependence since $\dot{Q} \propto STI \propto T^2 I \propto I^5$. We have investigated this explanation but found that it does not agree well with the measured data. Since the measurements are performed at room temperature (300K) and only a few Kelvin temperature increase due to Joule heating are measured the impact on the Peltier heating/cooling is negligible (see section 1 in the Supporting Information). The temperature increase is also taken into account in the COMSOL calculation of the Peltier heating/cooling, which solves for the full thermoelectric equation ($\rho C_p \boldsymbol{u} \nabla T = \nabla(k\nabla T - P\boldsymbol{J}) + Q$, see also Supporting Information but COMSOL modeling results in only a small deviation of about 2% from the linear exponent (see inset Figure 3b), which is about two orders lower than observed in the experiment.

While a heatdrift in the constriction due to high drift currents agrees well with our data and explains the observed deviation from a linear current dependency expected from the Peltier effect, other higher order causes are possible and further investigation of this effect will be necessary.

To summarize, we observe a strong geometrical dependence of both the Peltier and the Seebeck effect in graphene nanoconstrictions dominating over the previously reported thermoelectric effect at the graphene-metal interface.[4,20] We can explain this local variation of the Seebeck coefficient by a reduction in the EMFP, which is caused by the increased scattering from the edges. Compared to Au nanowires that have shown a similar effect previously,[15] graphene offers a more straightforward method of influencing the mean free path, due to its lower dimensionality and also comparatively bigger electron mean free path. Furthermore, we observe an additional contribution to the Peltier effect by an 'electron wind' resulting from the high drift velocity of charge carriers in the constriction. This work highlights the major influence of disorder and geometry on thermoelectric properties of graphene. Thus, thermoelectric effects are likely present in graphene whenever edge scattering becomes appreciable and can lead to undesired heating/cooling. Similarly, any temperature gradient across an edge scattering region will create a parasitic voltage drop over the device. These are important consideration for future photothermoelectric as well as thermal and electrical transport measurements in nanoscale electronic devices.

In addition, our findings have implications for thermal management in future integrated circuits made out of graphene: The results open a path to producing a single material thermocouple or Peltier element that can be precisely positioned using electron beam lithography. As shown in Figure S13 in the Supporting Information, a substantial reduction of the channel width effectively creates a highly localized Peltier element which could be used for local cooling or temperature

sensing. Such all-graphene thermocouples could be integrated into planar device structures on a wafer scale and at comparatively low costs.

Methods

Device fabrication

The devices were fabricated by transferring two different types of CVD graphene,[30] multilayer (2-4 layers) and single layer (see Supporting Information), on top of a Si chip with a 300 nm SiO_2 and pre-patterned Cr/Au contacts using a standard wet transfer method.[31] Subsequently, the graphene was patterned into the different geometries employing standard electron-beam lithography and then etched into different geometries using oxygen plasma etching.

Scanning Thermal Microscopy measurement methods

The SThM is located in a high vacuum environment, prohibiting parasitic heat transfer between the tip and the sample to achieve a better thermal resolution.[18,32] In our measurements, the spatial resolution is limited by the size of the tip-sample contact which is on the order of tens of nanometers.

We used two distinct scanning measurement methods, passive SThM temperature probing and active heated-probe local thermovoltage measurements.

In the Peltier measurement, the device is electrically excited with an AC bias V_{bias} through the global contacts at a frequency of f = 17Hz. The SThM tip is scanned over the sample, measuring the temperature $\Delta T_{\mathrm{peltier}}$ at the first harmonic (f) using a SRS830 lock-in (see Figure 1a). Simultaneously the unmodulated temperature-dependent DC signal and the Joule heating signal $\Delta T_{\mathrm{joule}}$, measured at the second harmonic ($2f$), are recorded. The Peltier and Joule measurements

were performed following Menges *et al.*,[18] to exclude tip-sample contact-related artefacts (see section 7 in the Supporting Information and [18]).

In contrast, for the thermovoltage scanning method, the SThM tip is heated up by applying a high AC voltage of $V_{\mathrm{heater}} = 2.24\ V_{\mathrm{pp}}$ to the temperature sensor. This Joule heating of the SThM tip at a frequency of f_{T} = 57Hz, results in a modulation of the SThM resistor temperature of approximately 60K, leading to a SThM tip temperature modulation of $\Delta T \approx 18 \pm 2\ \mathrm{K}$ at the interface with graphene (see section 7 Supporting Information). This local heat source is then scanned over the sample while the global voltage drop V_{th} over the two contacts is measured with a SR560 voltage pre-amplifier and a SRS830 lock-in amplifier at the second harmonic ($2f_{\mathrm{T}}$) (see Figure 1b). Our thermovoltage measurements do not require electrical contact between the tip and the sample, as does a similar method reported previously,[33] and thereby eliminate linked uncertainty, as well as requirements on the strength of the electrical tip-sample contact. To rule out effects on the measured signal stemming from accidental phase errors in the lock-in signal, we performed a DC measurement where a positive and negative square wave are applied respectively and the two resulting temperature maps are subtracted. This configuration shows the same signal as the AC measurements, thereby eliminating the possibility of an unintended phase effect causing the signal (see Supporting Information).

ASSOCIATED CONTENT

Supporting Information.

The Supporting Information is available free of charge from the ACS website and DOI. Peltier correction terms, graphene characterization, EMFP evaluation, *I-V* traces, DC measurement, thermovoltage measurements, SThM setup, FE analysis, current dependencies other geometries, long ribbon geometry, spatially dependent Seebeck coefficient theory, gate dependency, heat movement by carriers, island geometry measurements, sample preparation. (PDF)

AUTHOR INFORMATION

Corresponding Author

*Email: p.gehring@udelft.nl; o.kolosov@lancaster.ac.uk

Author Contributions

‖ A. H. and J. S. contributed equally to this work.

A.H. fabricated the devices. A.H., P.G. and O.K. drafted the manuscript. A.H. J.S., C.E. and P.G. performed the measurements. A.H. J.S., C.E., P.G., J.M. and O.K. analyzed and processed the data. Y.S. and J.W. provided the graphene. E.M. carried out the theoretical modelling and J.S. performed the FEM calculations. O.K. and P.G. supervised, conceived and designed the experiments. All authors discussed the results and contributed to manuscript revision. ‡These authors contributed equally. (match statement to author names with a symbol)

Funding Sources

This work is supported by the UK EPSRC (grant nos. EP/K001507/1, EP/J014753/1, EP/H035818/1, EP/K030108/1, EP/J015067/1, and EP/N017188/1).

Notes

The authors declare no competing financial interest.

ACKNOWLEDGMENT

The authors would like to thank Prof. Colin Lambert and Dr. Hatef Sadeghi for helpful discussions and Jasper Fried for performing the long ribbon conductance measurements. P.G. acknowledges a Marie Skłodowska-Curie Individual Fellowship under grant TherSpinMol (ID: 748642) from the European Union's Horizon 2020 research and innovation programme. O.K. acknowledges the EPSRC project EP/K023373/1 and EU project No.604668 QUANTIHEAT.

ABBREVIATIONS

SThM, scanning thermal microscope; EMFP, electron mean free path; AFM, atomic force microscopy.

REFERENCES

(1) B. Poudel, Q. Hao, Y. Ma, Y. Lan, A. Minnich, B. Yu, X. Yan, D. Wang, A. Muto, D. Vashaee, X. Chen, J. Liu, M. S. Dresselhaus, G. Chen, Z. Ren, *Science* **2008**, *320*, 634.

(2) L.-D. Zhao, S.-H. Lo, Y. Zhang, H. Sun, G. Tan, C. Uher, C. Wolverton, V. P. Dravid, M. G. Kanatzidis, *Nature* **2014**, *508*, 373.

(3) F. J. DiSalvo, *Science* **1999**, *285*, 703.

(4) K. L. Grosse, M.-H. Bae, F. Lian, E. Pop, W. P. King, *Nat. Nanotechnol.* **2011**, *6*, 287.

(5) X. Xu, N. M. Gabor, J. S. Alden, A. M. Van Der Zande, P. L. McEuen, *Nano Lett.* **2010**, *10*, 562.

(6) K. Behnia, *Fundamentals of Thermoelectricity*, Oxford University Press, **2015**.

(7) L. D. Hicks, M. S. Dresselhaus, *Phys. Rev. B* **1993**, *47*, 12727.

(8) L. D. Hicks, M. S. Dresselhaus, *Phys. Rev. B* **1993**, *47*, 16631.

(9) T. C. Harman, P. J. Taylor, M. P. Walsh, B. E. LaForge, *Science* **2002**, *297*, 2229.

(10) R. Venkatasubramanian, E. Siivola, T. Colpitts, B. O'Quinn, *Nature* **2001**, *413*, 597.

(11) M. Ibáñez, Z. Luo, A. Genç, L. Piveteau, S. Ortega, D. Cadavid, O. Dobrozhan, Y. Liu, M. Nachtegaal, M. Zebarjadi, J. Arbiol, M. V. Kovalenko, A. Cabot, *Nat. Commun.* **2016**, *7*, 10766.

(12) M.-J. Lee, J.-H. Ahn, J. H. Sung, H. Heo, S. G. Jeon, W. Lee, J. Y. Song, K.-H. Hong, B. Choi, S.-H. Lee, M.-H. Jo, *Nat. Commun.* **2016**, *7*, 12011.

(13) D. Dragoman, M. Dragoman, *Appl. Phys. Lett.* **2007**, *91*, 203116.

(14) Devender, P. Gehring, A. Gaul, A. Hoyer, K. Vaklinova, R. J. Mehta, M. Burghard, T. Borca-Tasciuc, D. J. Singh, K. Kern, G. Ramanath, *Adv. Mater.* **2016**, *28*, 6436.

(15) P. Zolotavin, C. I. Evans, D. Natelson, *Nanoscale* **2017**, *9*, 9160.

(16) Y. M. Zuev, J. S. Lee, C. Galloy, H. Park, P. Kim, *Nano Lett.* **2010**, *10*, 3037.

(17) A. Majumdar, *Annu. Rev. Mater. Sci.* **1999**, *29*, 505.

(18) F. Menges, P. Mensch, H. Schmid, H. Riel, A. Stemmer, B. Gotsmann, *Nat. Commun.* **2016**, *7*, 10874.

(19) W. Jeong, K. Kim, Y. Kim, W. Lee, P. Reddy, *Sci. Rep.* **2015**, *4*, 4975.

(20) I. J. Vera-Marun, J. J. van den Berg, F. K. Dejene, B. J. van Wees, *Nat. Commun.* **2016**, *7*, 11525.

(21) P. Tovee, M. Pumarol, D. Zeze, K. Kjoller, O. Kolosov, *J. Appl. Phys.* **2012**, *112*, 114317.

(22) W. Sun, H. Liu, W. Gong, L.-M. Peng, S.-Y. Xu, *J. Appl. PhysicsJ. Appl. Phys. J. Appl. 2Physics4884735J. Appl. Phys. J. Appl. Phys.* **2011**, *110*, 236101.

(23) L. Banszerus, M. Schmitz, S. Engels, M. Goldsche, K. Watanabe, T. Taniguchi, B. Beschoten, C. Stampfer, *Nano Lett.* **2016**, *16*, 1387.

(24) J. Baringhaus, M. Settnes, J. Aprojanz, S. R. Power, A. P. Jauho, C. Tegenkamp, *Phys. Rev. Lett.* **2016**, *116*, 186602.

(25) Y. Anno, Y. Imakita, K. Takei, S. Akita, T. Arie, *2D Mater.* **2017**, *4*, 025019.

(26) Q. Li, S. Das Sarma, *Phys. Rev. B - Condens. Matter Mater. Phys.* **2013**, *87*, 085406.

(27) A. H. Castro Neto, F. Guinea, N. M. R. Peres, K. S. Novoselov, A. K. Geim, *Rev. Mod. Phys.* **2009**, *81*, 109.

(28) Y. M. Zuev, W. Chang, P. Kim, *Phys. Rev. Lett.* **2009**, *102*, 096807.

(29) M.-H. Bae, S. Islam, V. E. Dorgan, E. Pop, *ACS Nano* **2011**, *5*, 7936.

(30) Y. Sheng, Y. Rong, Z. He, Y. Fan, J. H. Warner, *Nanotechnology* **2015**, *26*, 395601.

(31) X. Li, W. Cai, J. An, S. Kim, J. Nah, D. Yang, R. Piner, A. Velamakanni, I. Jung, E. Tutuc, S. K. Banerjee, L. Colombo, R. S. Ruoff, *Science* **2009**, *324*, 1312.

(32) K. Kim, W. Jeong, W. Lee, P. Reddy, *ACS Nano* **2012**, *6*, 4248.

(33) B. Lee, K. Kim, S. Lee, J. H. Kim, D. S. Lim, O. Kwon, J. S. Lee, *Nano Lett.* **2012**, *12*, 4472.

Supporting Information: Geometrically Enhanced Thermoelectric Effects in Graphene Nanoconstrictions

Achim Harzheim, Jean Spiece, Charalambos Evangeli, Edward McCann, Vladimir Falko, Yuewen Sheng, Jamie H. Warner, G. Andrew D. Briggs, Jan A. Mol, Pascal Gehring, and Oleg V. Kolosov**

This supporting information contains:

Supplementary figures S1-S12 and supplementary texts chapter 1-13

1. Peltier correction due to Joule heating

Since the Peltier coefficient is proportional to the temperature squared, the Joule heating in our devices undeniably has an influence on the measured Peltier heating/cooling. From the measurements of Joule heating in our bow tie devices, an increase of $\Delta T_{\mathrm{joule}} \leq 10\ \mathrm{K}$ can be extracted.[1] Using this value, we can estimate the expected contribution of Joule heating to the Peltier heating/cooling measured. The heat generated or taken away by the Peltier effect is given as

$$\dot{Q} = \Pi I = STI = \beta T^2 I, \tag{S1}$$

Where $\beta = -\frac{\pi^2 k_B^2}{3\epsilon_F e}\left[1 + n\,U\frac{l(x)}{l_0} - (n-1)U\right]$ is the part of the Mott formula independent of the temperature. Then assuming $T = T_0 + \Delta T_{\mathrm{joule}}$ with $T_0 = 300K$ being the room temperature and $\Delta T_{\mathrm{joule}} = 10\ \mathrm{K}$ the maximum increase in temperature due to Joule heating, $\dot{Q}_{corr} = \beta\left(T_0 + \Delta T_{\mathrm{joule}}\right)^2 I = \beta\left(T_0^2 + T_0\Delta T_{\mathrm{joule}} + \Delta T_{\mathrm{joule}}^2\right)I$.

We can then calculate the percentage increase of heat and thereby the temperature due to the correction for the Joule heating as follows:

$$\Delta T_{\mathrm{correction}} = \frac{\dot{Q}_{\mathrm{corr}} - \dot{Q}_{\mathrm{original}}}{\dot{Q}_{\mathrm{original}}} = \frac{\beta\left(T_0^2 + 2T_0\Delta T_{\mathrm{joule}} + \Delta T_{\mathrm{joule}}^2\right)I - \beta T_0^2 I}{\beta T_0^2 I} = \frac{\left(T_0^2 + 2T_0\Delta T_{\mathrm{joule}} + \Delta T_{\mathrm{joule}}^2\right) - T_0^2}{T_0^2} = \frac{96100 - 90000}{90000} \approx 6.8\% \tag{S2}$$

2. Graphene characterization

In order to characterize the graphene, Raman spectroscopy and SEM imaging was employed. Pre-patterning SEM images showed continuous coverage and a domain size of roughly $10\ \mu\mathrm{m}$ while the Raman spectroscopy allowed us to conclude the number of layers and quality of the graphene employed. As shown in Figure S1a, the ratio of the G to 2D peak indicates single layer graphene, with a certain degree of disorder not unusual for CVD graphene as is evident by the visible D peak. The graphene shown in Figure S1b on the other hand is clearly multiple layers as the G peak is higher than the 2D peak.

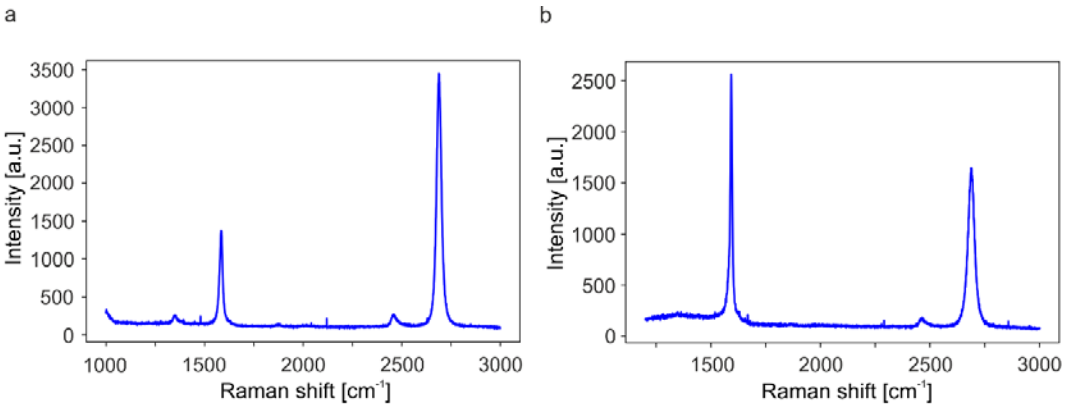

Figure S1. Raman spectroscopy of the graphene used. (a) 1-2 layer graphene and (b) few layer graphene

3. Evaluation of the electron mean free path

In order to extract the bulk EMFP l_0 for the left and right reservoir, long 3 µm wide ribbons are used, which are the same width as the reservoirs and therefore give a good estimate. The bulk EMFP l_0 can be calculated from a gate trace, where the current through the ribbon at a constant voltage is measured as the gate is swept.[2] In graphene, a curve with a minimum at the Dirac point is expected, as shown in Figure S2a.

Using the transconductance from this measurement, dG/dV_g, to estimate the carrier mobility gives:

$$\mu = \frac{dG}{dV_G}\frac{L}{WC_{\mathrm{ox}}}, \tag{S3}$$

where $L = 43$ µm is the ribbon length, $C_{ox} = \frac{\epsilon_0 \epsilon_r}{d}$ is the back gate capacitance ($\epsilon_r = 3.9$ and $d = 300$ nm for our samples) and $W = 3$ µm the width of the ribbon.[3] We can then calculate the mean free path with Equation S3 from

$$l_e = \frac{\hbar}{e}\mu\sqrt{n\pi}, \tag{S4}$$

with the carrier concentration $n = \frac{C_{\mathrm{ox}}(V_g - V_{\mathrm{dirac}})}{e}$ given by the position of the dirac point V_{dirac}. Six different ribbons (one ribbon is displayed in Figure S2 a, b and c) were measured that gave an average of $\mu = 8700 \pm 100\ cm^2(Vs)^{-1}$ and $l_e = 226 \pm 20$ nm at $V_g = 0$.

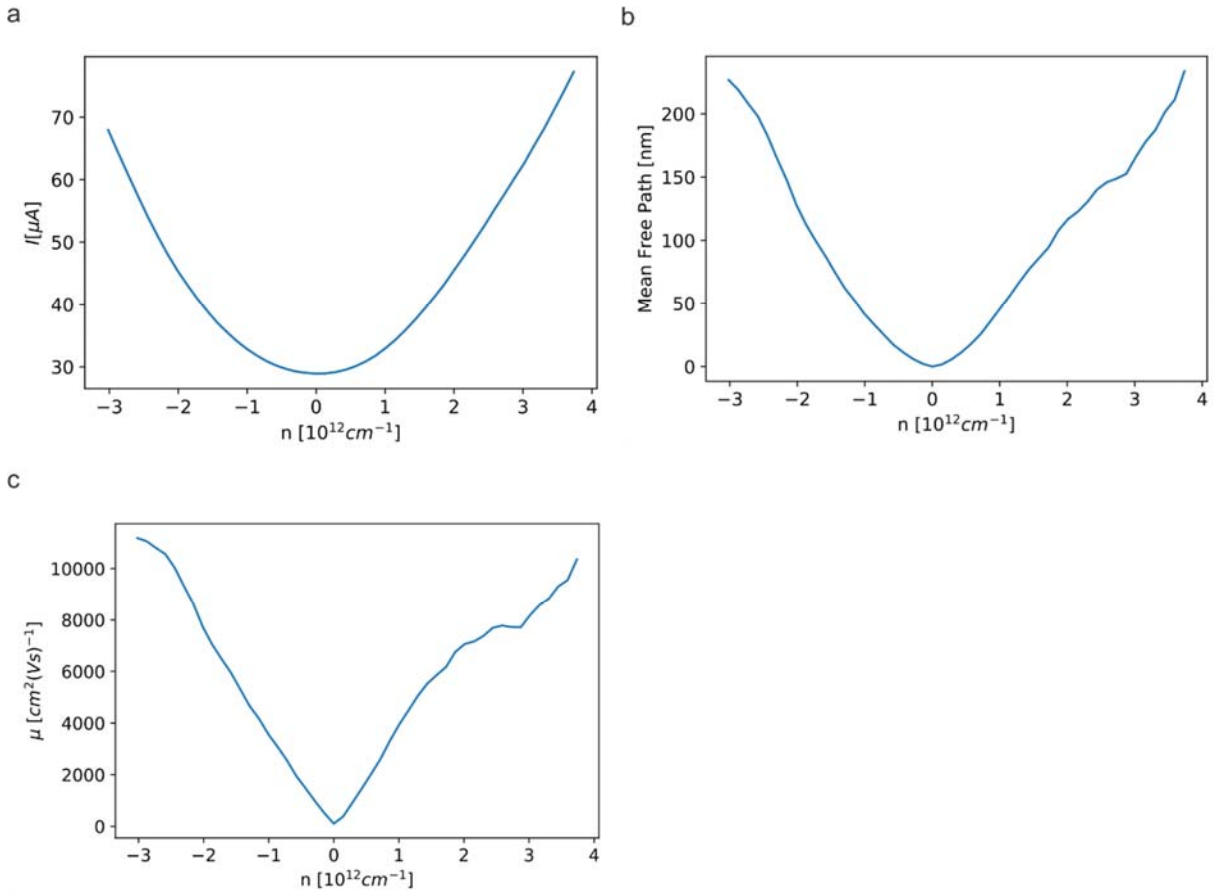

Figure S2: Bulk EMFP extracted from long ribbon back-gate dependent gatetraces. (a) Representative gate dependent current measurement of a device as a function of the carrier density. (b) calculated EMFP as a function of the carrier density using the data in a and Equation S4. (c) Extracted mobility μ as a function of carrier density using the data in a and Equation S3.

4. *I-V* characteristics

All of the devices measured show linear or minimal deviation from linear *I-V* characteristics within the probed voltage bias as is shown in Figure S3. This rules out another possible reason for the observed Peltier effect, a highly resistant bridge or mobility gap due to the constriction that would induce a change in the Seebeck coefficient as predicted previously.[4] Such a mobility band gap would be reflected in a nonlinear *I-V*

dependence at low currents that is not observed in our measurements. In addition, as we are measuring in the linear *I-V* regime *V* and *I* differ by a constant multiplier, the resistance and nonlinear effects do not influence the measurements. The voltage applied during Peltier measurements is typically $V_{\mathrm{bias}} = 2V_{\mathrm{pp}}$ for the shown samples, corresponding to a current of $I_{\mathrm{bias}} = 25 - 30\mu\mathrm{A}$ for multi-structured devices and around $I_{\mathrm{bias}} = 30 - 90\mu\mathrm{A}$ for the bow tie devices. We have similarly recorded IV curves of our bow-tie devices at high applied DC voltages. These devices are showing slight non-linear behavior at higher voltages, but are still well approximated as being in the linear regime and in addition, show a symmetric current response. A typical device IV-curve is shown below in Figure S3 d. All device resistances were on the order of kΩs and were biased at sufficiently low voltages to exhibit linear IV characteristics.

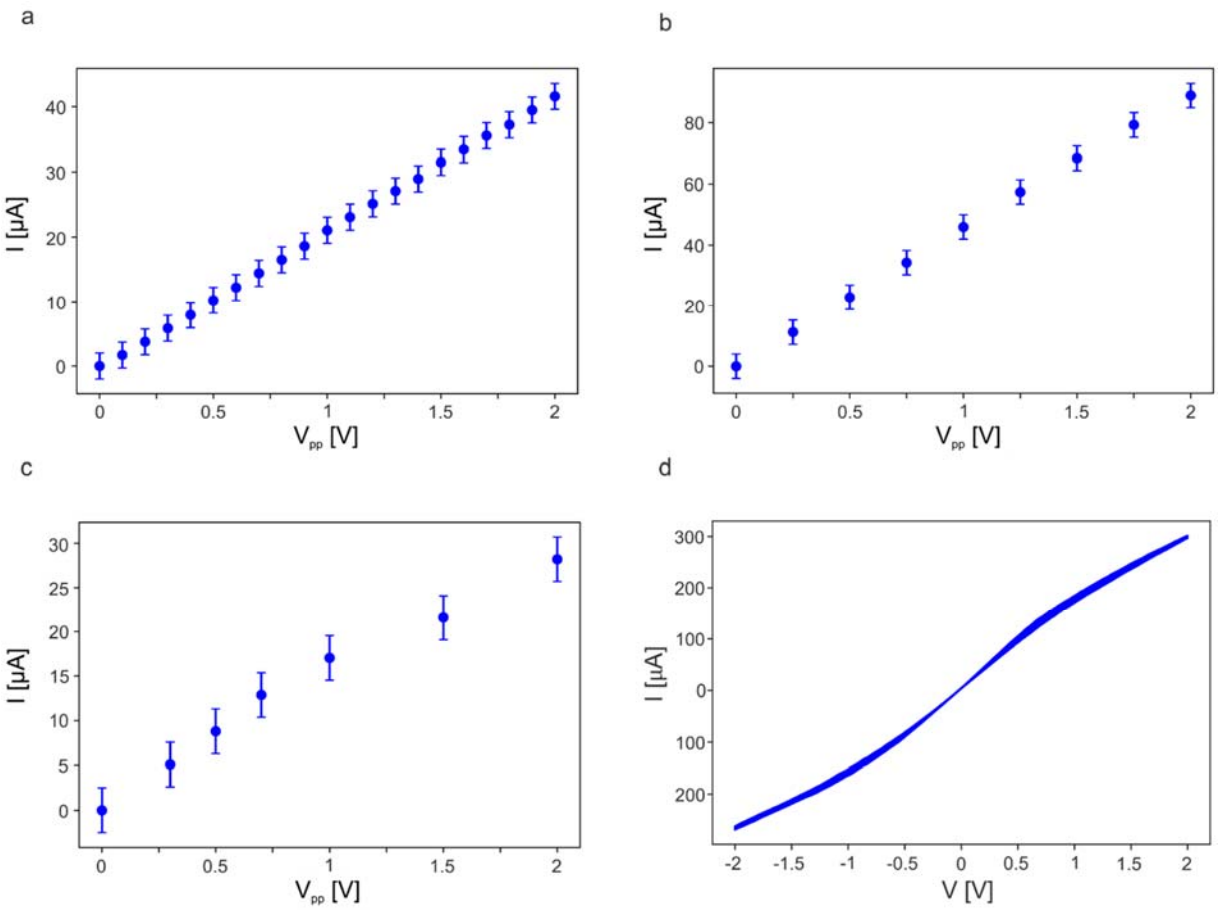

Figure S3: AC *I-V* traces for the different devices shown in this paper in a,b,c and a typical DC trace seen in our devices in d. (a)

Device 3 shown in Figure 2 and 3. (b) Device 1 shown in Figure 1. (c) long wire device show in Figure S8. (d) DC IV trace going to high currents and biases. While the current does not quite stay linear, no pronounced asymmetry is visible.

5. DC thermal measurements

In order to eliminate any interpretation of measured phase as the origin of the observed Peltier heating and cooling effects, a quasi-DC measurement of the Joule heating is performed. A step function at $1\ V_{pp}$ is applied to the device at a low frequency while the temperature response is recorded. This is a pure temperature recording without a phase dependency to separate Peltier heating/cooling and Joule heating. Subsequently, a second measurement with $-1\ V_{pp}$ is performed and subtracted from the first measurement. Since the Joule heating is symmetric with respect to the constriction, subtracting the two measurements eliminates the Joule heating signal. The Peltier heating on the other hand is asymmetric and the result is a purely Peltier heating/cooling map that then has to be divided by two. As can be seen in Figure S4, the resulting DC Peltier signal reproduces the AC measurements well.

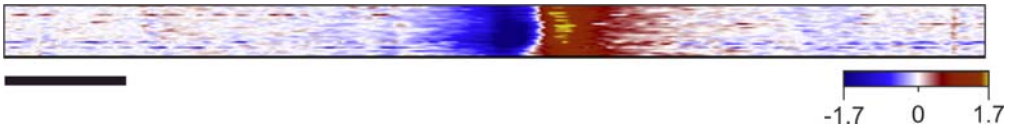

Figure S4: DC measurement of a bow tie junction. The image is created by subtracting a positive and a negative image. The scale bar is 500 nm.

6. Bow tie structure - thermovoltage measurements

The thermovoltage of the bow tie device in Figure 1 was measured with the hot (18 K heater excess temperature) tip scanning over the device as explained in the experimental section of the main manuscript and in section 7 below.[5] For the thermovoltage measurements we observe the same features as in the Peltier measurements, with a positive and negative thermovoltage on the respective sides of the junction and a zero signal node in between (see Figure S5). This is a further

confirmation that it is a change in the Seebeck coefficient rather than a current induced effect that is responsible for the observed signal.

Figure S5: Thermovoltage measurement of Device 1. The thermovoltage map resembles largely the Peltier map. The scale bar is 500 nm.

7. SThM measurement setup

In order to gain insights into a sample's heat dissipation properties, we deploy Scanning Thermal Microscopy (SThM) that uses a standard AFM feedback loop to maintain a constant force between the sample and the probe.[6] Acting as both a sensor and a heater, the SThM probe consists of a two-legged Si cantilever with a doped Si heater above a conical tip.

Prior to measurement, the probe electrical resistance is calibrated as a function of the temperature and the probe excess temperature arising from self-heating of the heater is quantified for a given electrical power.[7] This also allows us to quantify the thermal resistance of the cantilever R_p. We obtained values of R_p between $6x10^4$ to $1.2x10^5$ KW^{-1} for the probes used in these experiments.

During thermometry experiments, the probe resistance is monitored *via* a modified Wheatstone bridge whose output is amplified before being fed into a lock-in amplifier (Stanford Research Systems, SR-830). A combined AC+DC bias voltage is applied on the bridge. The AC component (91 kHz) provides high sensitivity through lock-in detection and the DC part creates Joule heating in the probe heater. We used a DC offset

generating 26 K excess temperature with respect to the surrounding. When the probe is brought into contact with the sample surface, it cools down (heats up) depending on the increase (decrease) of the heat flux to the sample and consequently on the sample local heat transport characteristics. The variations of the probe heater temperature generate variations of the probe electrical resistance, which are detected by the electronics. Obtaining temperature maps of operating devices can be challenging as the probe-sample contact varies and creates artefact in the temperature measurement. To counter such effects, Menges *et al.*[1] developed a method taking into account the heat flux from a heated tip to the sample and correcting the measured temperature map. This is realized by creating an oscillating temperature field in the sample through an applied AC bias on the device. The AC temperature variations can be detected by the SThM sensor and amplified by lock-in detection. Then a corrected temperature map is obtained by:[1]

$$\Delta T_{sample} = \Delta T_{sensor_0} \frac{\Delta V_{AC}}{\Delta V_{AC} - \Delta V_{DC}} \quad \text{(S5)}$$

where ΔT_{sample} is the sample temperature rise, ΔT_{sensor_0} is the SThM heater excess temperature before contacting the sample, ΔV_{AC} is the variation of the SThM signal measured at the device AC driving frequency and ΔV_{DC} is the variation of the SThM signal sensitive to tip-sample heat fluxes. To measure Peltier temperature changes, ΔV_{AC} is measured at the driving frequency (first harmonic) while to measure Joule heating ΔV_{AC} is measured at twice this frequency (second harmonic).

During scanning thermovoltage (scanning thermal gate microscopy, SThGM) experiments, the same setup is used but the AC bias on the Wheatstone bridge has a lower frequency (57 Hz). Since our probe has a time constant below 1ms, one order of magnitude faster than the AC frequency, it is ensured that we reach thermal equilibrium throughout each AC cycle. The temperature generated in the probe heater varies from 0 to 40 K. Tovee *et al.* have shown that low thermal conductivity materials (< 2-5 W (m k)$^{-1}$) can get locally heated by a hot tip.[7] To quantify this heating and obtain a local Seebeck coefficient, we need to estimate the

temperature at the tip-sample contact. As we know the cantilever thermal resistance we can deduce the measured thermal resistance between the heater and the sample R_m. The latter is the sum of 3 components: the thermal resistance of the silicon conical tip R_{tip}, the interface resistance between the tip and the sample R_{int} and the thermal spreading resistance within the sample R_{spr}. Estimate of R_{spr} are obtained from analytical formula of a circular heat source on a layer on substrate.[8,9] R_{tip} and R_{int} are relatively unknown even if models exist.[10] However, as we measure the total resistance R_m between the heater and the sample, we can obtain the sum $R_{tip} + R_{int} = R_m - R_{spr}$ and deduce the temperature at the sample surface from

$$\Delta T = \Delta T_{heater} \frac{R_{spr}}{R_m}. \quad \text{(S6)}$$

With our measurements, we obtained $\Delta T = 18 \pm 2$ K.

It is worth noting here, that the Peltier heating/cooling source is distributed. Since the Seebeck coefficient is spatially dependent on the mean free path (see section 11), a signal is expected as soon as the edge disorder and defects become appreciable. However, while the source is distributed, the weight of Peltier heating/cooling is not constant but rather increases with a narrower constriction in accordance with the sharply decreasing thermopower (see Figure S11). Therefore, the majority of heating/cooling is taking place in the narrowest part of the constriction (the reason for a node in the middle of the constriction is that the Peltier switches from heating to cooling) and is decaying as the width of the constriction increases.

A second factor defining the shape of the signal in the measurements is the spreading of heat in our sample. Our SThM measurement on device without self-heating show that heat dissipation from the heated tip in the areas with and without graphene differs by less than 5%, with limited broadening of the graphene/ SiO_2–SiO_2boundary (see Figure S6). This suggests that it is reasonable to assume that the SiO_2/Si substrate plays the dominant role in the heat spreading. This is similar to previous measurements that suggest that heat spreading in single-layer graphene on $SiO_2$is poor, and in our case below the characteristic dimensions of a 100nm constriction.[11]

In addition, we can consider a phonon mean free path of around 100 nm.[12] While graphene is decoupled from the oxide due to the interface resistance it still interacts strongly with the substrate, which is why the thermal conductivity (and the mean free path) are greatly reduced.[13] Therefore, as the Peltier heat gets carried away in the lattice by phonons, it interacts with the substrate/impurities/edges over a length scale of 100 nm or smaller. We observe a temperature distribution decaying up to 1 μm from the constriction as a result of this heat spreading, which is within ten times the mean free path.

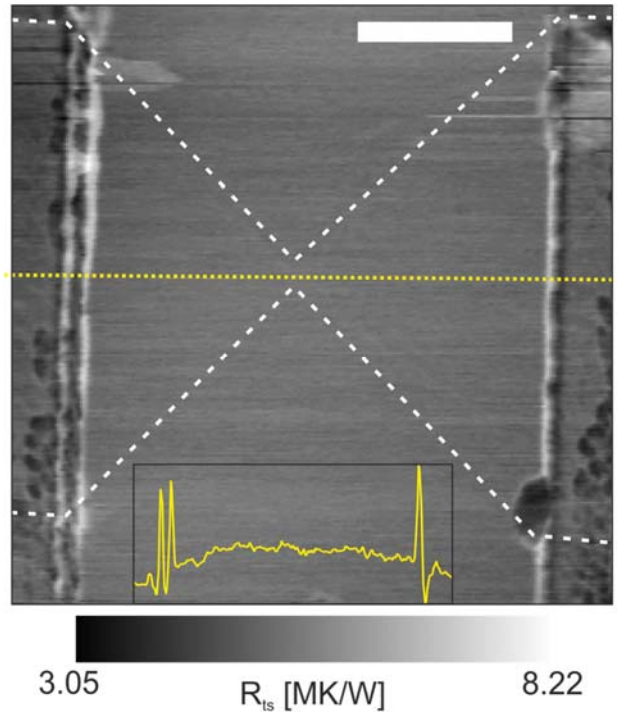

Figure S6: SThM map of the tip-sample thermal resistance (R_{ts}) of a device without excitation. The contrast between graphene and SiO_2 is difficult to make out in the image as the heat dissipation does not change much. In addition, the constriction does not affect the spreading much either as can be seen from the linecut shown in the inset (yellow line), where the spikes and big changes are the contacts on the left and right. The scale bar is 1 μm.

8. Finite Elements Analysis

To compare the modelled Seebeck coefficient distribution (see section 11) and the subsequent Peltier effect with experimental results, we turned to Finite Element Analysis (FEA) using COMSOL MULTIPHYSICS©. Realistic 3D models included heat transfer in solid, electrical current and multiphysics effects, e.g. thermoelectric effects. Dimensions of the models were set large enough (10 µm) compared to the device (< 3 µm) to avoid any dimensional artefact in the results. As the device is resting on a 300 nm silicon oxide on silicon, with thermal conductivity of silicon much higher than the one for SiO_2 we assumed that the silicon was acting as a thermal bath. In addition, we assumed perfect coupling between the graphene and the oxide and predominantly diffusive heat transfer.

The main Equation system solved for this system is:

$$\begin{cases} \rho C_p \boldsymbol{u}\,\nabla T = \nabla(k\nabla T) + Q \\ \nabla \boldsymbol{J} = Q_j\,; \boldsymbol{J} = \sigma E + \boldsymbol{J_e}\,; \boldsymbol{E} = -\nabla V \\ \rho C_p \boldsymbol{u}\nabla T = \nabla(k\nabla T - P\boldsymbol{J}) + Q \end{cases} \tag{S7}$$

where ρ, C_p, k, σ are the materials properties of density, heat capacity and thermal and electrical conductivities, respectively. $T, Q, \boldsymbol{J}, \boldsymbol{E}, V$ are the temperature, heat density, current density, electric field and potential, respectively.

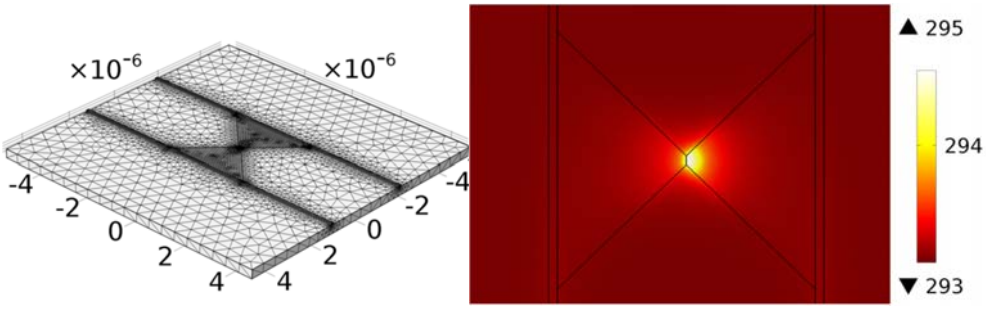

Figure S7: meshed geometry of the bow tie device (left) and modelled temperature field for a positive DC current (right). The asymmetric Joule heating seen on the right panel is due to the Peltier effect.

The geometry of the device is known from manufacturing and AFM measurements (Figure S7 a). The Seebeck coefficient modelled in the main text is set is for the graphene Seebeck coefficient and is thus position dependent. As the current was recorded during measurement, the only unknown parameters are the electrical and thermal conductivities of the graphene layer (we assume 1.4 $Wm^{-1}K^{-1}$ for the thermal conductivity of the silicon oxide). These two parameters will be assumed as fitting parameters to match the observed Joule heating as we explain here after.

We proceeded as follows. One side of the bow tie is grounded while to the other side we apply a DC current and calculate the resulting temperature field produced in the device. Then we change the polarity of the DC current. These temperature fields include both Peltier and Joule effects. To separate them, we extract modelled temperature profiles from both simulations and define the Peltier and Joule temperatures as

$$T_{Peltier}(x) = \frac{T_{DC^+}(x) - T_{DC^-}(x)}{2} \quad \text{(S8)}$$

$$T_{Joule}(x) = \frac{T_{DC^+}(x) + T_{DC^-}(x)}{2} \quad \text{(S9)}$$

Once we obtained a Joule heating temperature profile as in Figure S7 b, we can compare it to the data received from the SThM measurements. Using the same current in the FEA as in the experiments, we used the smallest Joule heating value $1\ V_{\mathrm{pp}}$ ($17.2\ \mu A$) to fit the modelled profiles to the measured ones by changing the electrical and thermal conductivities of the graphene layer. We obtained a good fit for realistic parameters of $120\ \mathrm{Wm^{-1}K^{-1}}$ and $5 \cdot 10^5\ \mathrm{Sm^{-1}}$. These fitting parameters are then used for all subsequent calculations such as the Joule heating at higher currents and the Peltier simulations.

9. Current dependency of the island and ribbon geometries

The behavior of the bowtie devices at high currents, where a change from a linear to a cubic current dependence is observed, is also seen in the other geometries studied. Again, the SThM tip is parked to the left or right side of a constriction where the signal due to a geometrical change is perceived highest in the map. Then the current through the device is ramped up as the signal strength is recorded. As shown in Figure S8, a combination of a linear and cubic dependence can be fitted to both the island and ribbon geometry, the crossover point observed at somewhat different current values within 50%. This is further evidence for a current induced origin of the enhancement of the Peltier effect.

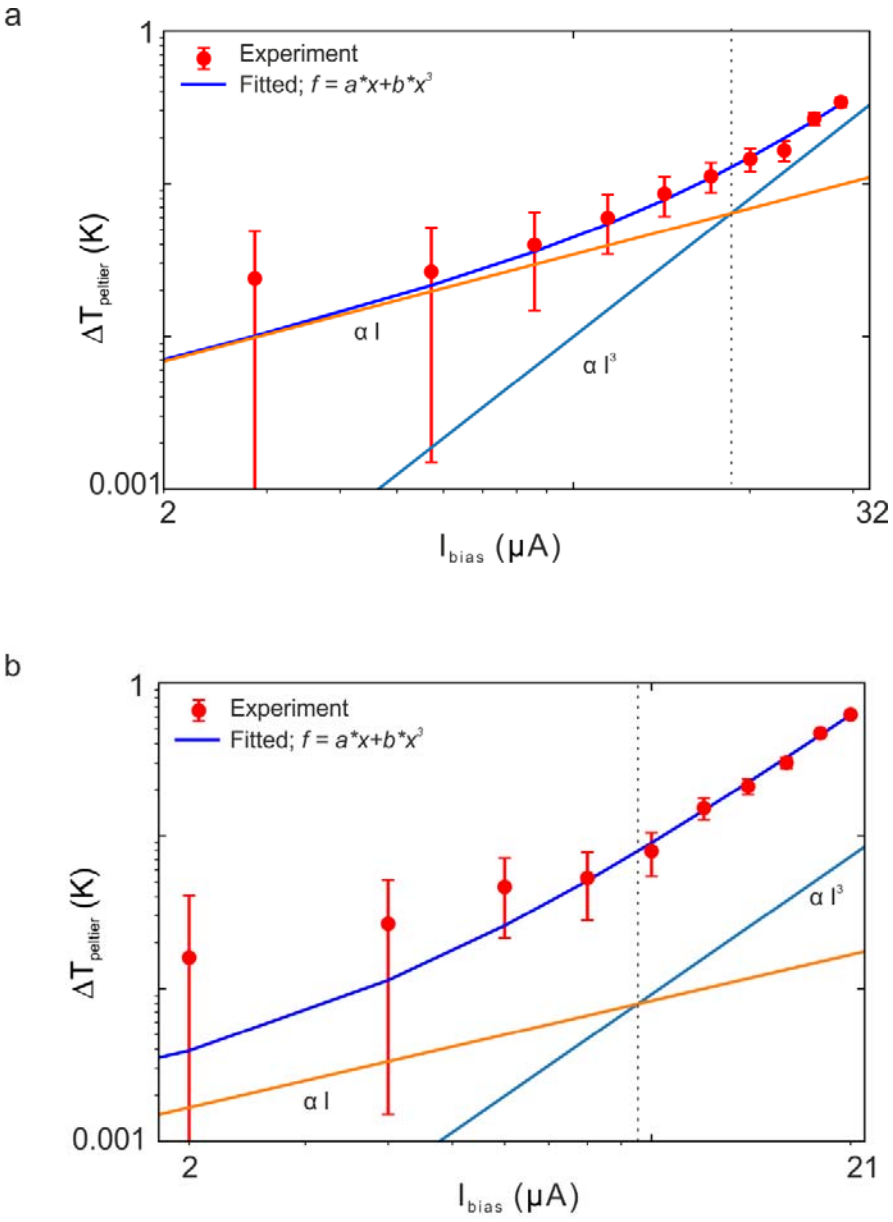

Figure S8: Current dependence measurements of the Peltier signal for (a) the island geometry and (b) the long ribbon.

10. Long ribbon:

The thermoelectric effects are prevalent in all geometries that were tested here, such as longer ribbons and island structures and is of comparable strength in all of them. In both the Peltier and thermovoltage measurements (Figure S9 a and b), a fine structure is showing, similar to previously observed effects in photocurrent nanoscopy of graphene that are attributed to charge puddles, defects and inhomogeneities,[14] in addition to the edge disorder prevalent in our samples due to the oxygen plasma fabrication step.

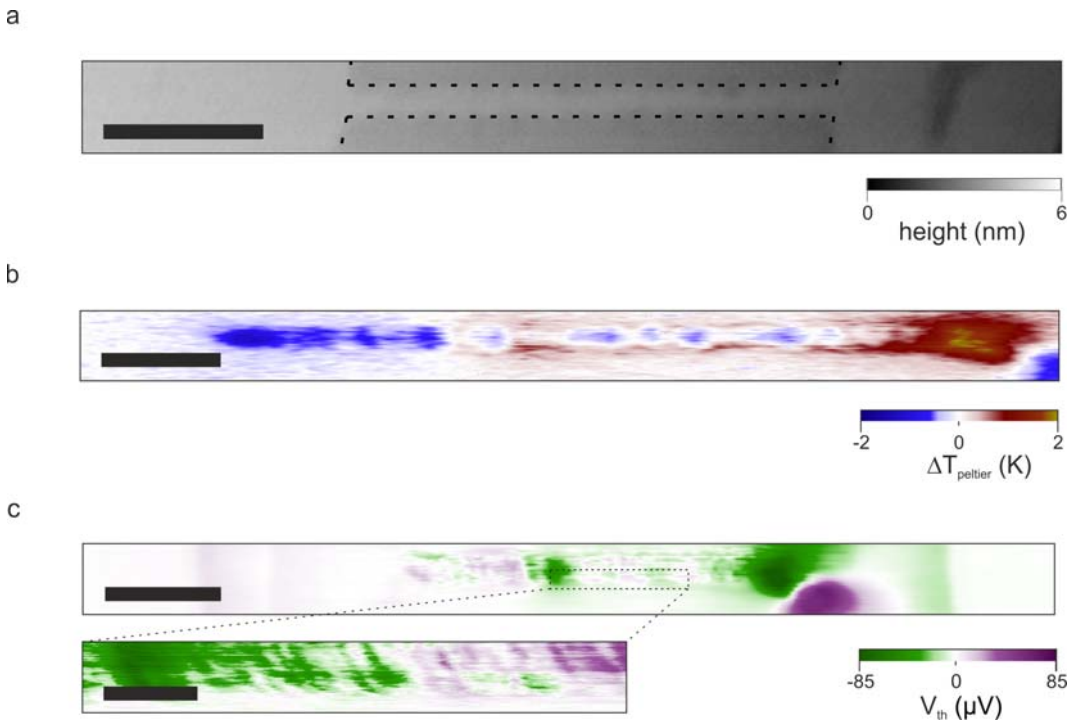

Figure S9: Thermoelectric measurements on the wire geometry. (a) Lateral Friction image of the wire geometry. (b) Peltier map of the wire geometry. Multiple sign changes in the middle of the ribbon are visible, in addition to a defect caused signal on the right. (c) Thermovoltage map of the wire geometry. Again, a strong signal is visible on the right-hand side of the device due to a defect and a fine structure is visible that is shown again in a close-up.

The scale bars are 500 nm in (a) and (c) in the main measurement, 250 nm in (b) and 100 nm in the close up in (c).

In all measurements, there is a stark effect at the boundary between bulk graphene and the sub 100 nm constriction, reinforcing the notion that the constriction itself is responsible for the effect. In order to show the high resolution and the fine structure in our measurements, a long graphene ribbon is investigated. In addition to a defect on the side that is causing a big signal, multiple sign changes and fine structures can be observed.

11. Spatially dependent Seebeck coefficient

We will start by giving a definition of electrical current in the linear response regime under an electric field or thermal bias. For electrical current density $\boldsymbol{j}$, the linear response in terms of the electric field $\boldsymbol{E}$ and the temperature gradient ΔT is given by

$$\boldsymbol{j} = \sigma \boldsymbol{E} - \sigma S \Delta T \,. \tag{S10}$$

where σ is the electrical conductivity, and S is the Seebeck coefficient describing the thermopower. We consider current along the x direction, $\boldsymbol{E} = -dV/dx$, and:

$$j_x = -\sigma \frac{dV}{dx} - \sigma S \frac{dT}{dx} \,. \tag{S11}$$

In the following, we explain how to calculate the spatial dependence of the Seebeck coefficient for a bowtie device by first considering its resistance. We begin with the diffusive conductance $G_d = \frac{2e^2}{h}\, k_F l \frac{W}{L}$ of a rectangular graphene device of length L in the longitudinal x direction and width W in the transverse y direction with mean free path l. In a bowtie geometry (shown in Figure S9), [15–17] the width of the device in the y direction varies from a maximum $Y = 2t + W$ to a minimum W.

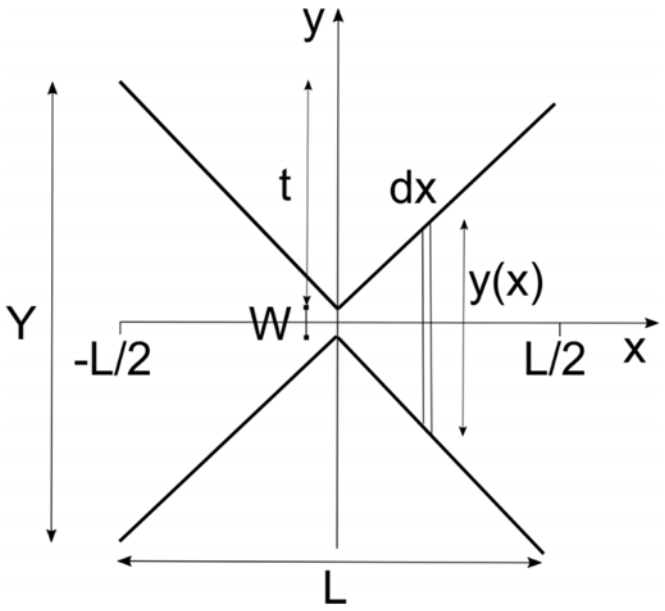

Figure S10. Schematic of the bowtie junction of length L, maximum width Y, minimum width W and constriction width y(x).

To determine the spatially-dependent resistance $R(x)$ and spatially-dependent Seebeck coefficient $S(x)$, we consider a thin strip of infinitesimal length dx located at length x from the centre of the constriction (where $x = 0$) and of width $y(x)$: on the right hand side, $0 \leq x \leq L/2$ and $W \leq y(x) \leq Y$.

We take into account two spatially-dependent effects: (i) a geometrical effect whereby the width change as a function of x is taken into account by replacing W in the diffusive conductance; (ii) a spatially dependent mean free path $l(x)$ to model scattering at edges which is relevant near the constriction.

In particular, we consider an infinitesimal strip of length dx located at position x on the right hand side $x \geq 0$, as depicted in Figure S10. The corresponding width $y(x)$ at that point is

$$y(x) = 4tx/L + W;\ 0 \leq x \leq L/2;\ W \leq y(x) \leq Y. \quad \text{(S12)}$$

This can then be used to write the conductance as

$$G(x) = \frac{2e^2}{h} k_F l(x) \frac{y(x)}{dx}, \tag{S13}$$

where $l(x)$ is a position dependent mean free path. We model it generically as

$$l(x) = l_0 \left[1 + c_n \left(\frac{l_0}{y(x)}\right)^n\right]^{-1} \tag{S14}$$

where l_0 is the bulk mean free path in our graphene devices and n and c_n are real numbers.

Thus, the contribution of the graphene strip to the resistance is

$$R(x) = \frac{h}{2e^2} \frac{1}{k_F l(x)} \frac{dx}{y(x)}. \tag{S15}$$

To determine the total resistance, we sum resistances in series by integrating with respect to x. Note that the EMFP is only explicitly affected by scattering in the transverse direction, hence the dependence on the width *y(x)* in Eq.(1). However, for the bow tie, *y(x)* is itself a function of *x* by geometry and, as we sum resistances in series in our derivation, we change variables from *y(x)* to *x* in order to integrate with respect to the variable *x*. The left hand side of the constriction gives the same contribution as the right, giving a factor of two, and the total resistance is

$$R = \frac{h}{2e^2} \int_0^{\frac{L}{2}} \frac{1}{k_F l(x)} \frac{dx}{y(x)} = \frac{h}{e^2} \frac{1}{k_F l_0} \int_0^{\frac{L}{2}} \frac{dx}{y(x)} \left[1 + c_n \left(\frac{l_0}{y(x)}\right)^n\right]$$

$$= \frac{h}{e^2} \frac{1}{k_F l_0} \left(\frac{L}{4t}\right) \int_W^Y dy \left[\frac{1}{y(x)} + c_n \frac{l_0^n}{y(x)^{n+1}}\right] = \frac{h}{e^2} \frac{1}{k_F l} \left(\frac{L}{4t}\right) \left[\ln\left(\frac{Y}{W}\right) + \frac{c_n l_0^n}{n} \left(\frac{1}{W^n} - \frac{1}{Y^n}\right)\right]$$

$$\approx \frac{h}{2e^2} \frac{1}{k_F l_0} \left(\frac{L}{Y}\right) \left[\ln\left(\frac{Y}{W}\right) + \frac{c_n}{n} \left(\frac{l_0}{W}\right)^n\right] \tag{S16}$$

where, in the last line, $Y \gg W$ was used. The first term is similar to the diffusive (Drude) resistance G_d^{-1} introduced earlier for a rectangular system and, for $n = 1$ and $c_n = 1$, the second term, due to 'boundary' scattering, is

$$R \approx \frac{h}{2e^2} \frac{1}{k_F W} \left(\frac{L}{Y}\right) \tag{S17}$$

In other words, the total resistance is approximately equal to a diffusive and a boundary scattering contribution.[18] This enables us to calculate the Seebeck coefficient by writing the Mott formula ($S = -\frac{\pi^2 k_B^2 T}{3e}\frac{1}{G(\epsilon)}\frac{dG(\epsilon)}{d\epsilon}|_{\epsilon=\epsilon_F}$) as

$$S = \frac{\pi^2 k_B^2 T}{3e}\frac{1}{R(\epsilon)}\frac{dR(\epsilon)}{d\epsilon}|_{\epsilon=\epsilon_F}, \quad \text{(S18)}$$

with

$R(\epsilon) \approx \frac{h}{2e^2}\frac{\hbar v}{\epsilon \ell_0}\left(\frac{L}{Y}\right)\left[\ln\left(\frac{Y}{W}\right) + \frac{c_n}{n}\left(\frac{l_0}{W}\right)^n\right]$, where we used $\epsilon = \hbar v k$.

We then find that

$$S = -\frac{\pi^2 k_B^2 T}{3e\epsilon_F}\frac{\left[(1+U)\ln\left(\frac{Y}{W}\right)+[1-(n-1)U]\frac{c_n}{n}\left(\frac{l_0}{W}\right)^n\right]}{\left[\ln\left(\frac{Y}{W}\right)+\frac{c_n}{n}\left(\frac{l_0}{W}\right)^n\right]}. \quad \text{(S19)}$$

Going back to the resistance of a strip in Equation S15,

$$R(x) = \frac{h}{2e^2}\frac{\hbar v}{\epsilon \ell_0}\left[\frac{1}{y(x)} + c_n\frac{l_0^n}{y(x)^{n+1}}\right]dx, \quad \text{(S20)}$$

we can determine local thermopower via Equation S18:

$$S(x) = -\frac{\pi^2 k_B^2 T}{3\epsilon_F e}\left[1 + n\,U\frac{l(x)}{l_0} - (n-1)U\right], \quad \text{(S21)}$$

where $U = \frac{d\ln l_0}{d\ln \epsilon}|_{(\epsilon=\epsilon_F)}$. This means that our Seebeck coefficient effectively changes due to the changing width in our constriction (see Figure S11), explaining the signal that is observed.

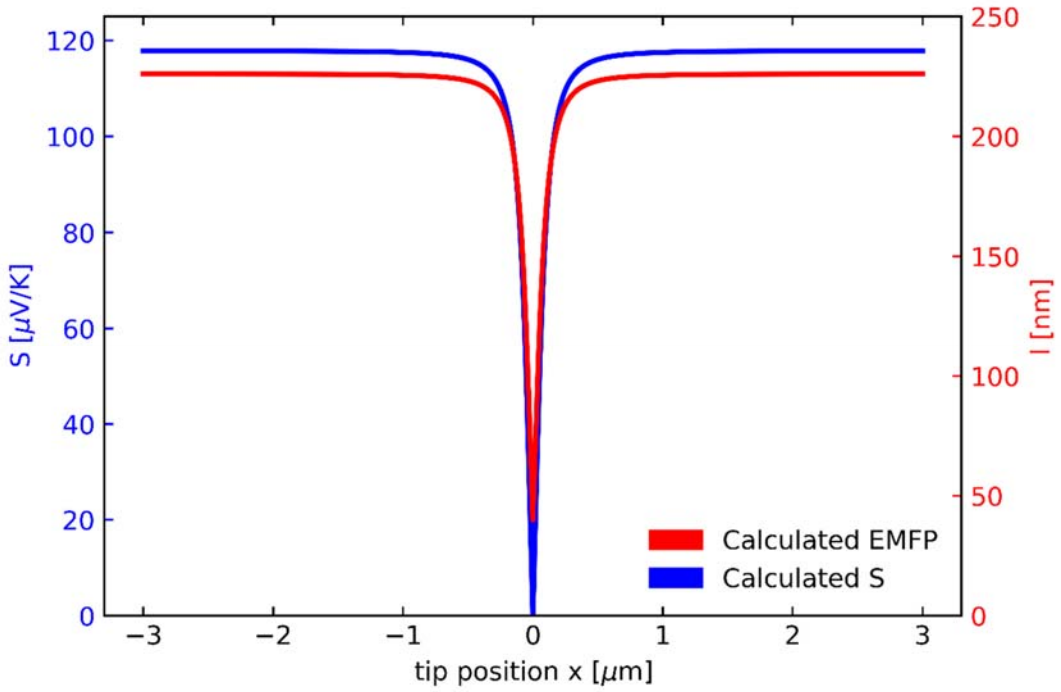

Figure S11. Calculated EMFP and Seebeck coefficient S for the bowtie constriction due to increased edge scattering for the fitting parameters obtained from Figure 2, giving a bulk mean free path of $l_0 \approx 226$ nm and S $\approx 118\ \mu VK^{-1}$.

Using this model with $n = 2.6$ and $c_n = 0.56$ and a bulk mean free path $l_0 = 226$ nm the EMFP is reduced substantially within our constriction region to about $40\ nm$ as shown below in Figure S10. This in turn reduces the Seebeck coefficient from $\approx 118\ \mu VK^{-1}$ to $\approx 0.35\ \mu VK^{-1}$ in our model, a change over 3 orders of magnitude. This is due to Equation (S21) involving a difference of terms; rather than a seemingly linear dependence on the mean free path, a small change in the EMFP can then result in a vastly differing Seebeck coefficient. It is also worth noting here, that for an almost ballistic sample where $n = 1$ and $l_0 \gg \Delta y$ the dependence of S on the width is just a linear one: $S \approx 1 + \frac{U\ \Delta y}{c_n l_0}$ but our fitting shows that we are in a diffusive/ballistic crossover regime instead. The bulk mean free path is extracted from gate dependent measurements of long ribbons as discussed earlier in section 3 and the fitting parameters n and c_n are obtained from a thermovoltage fit as explained in Figure 2.

12. Gate dependency

Through back gating of our devices, different carrier concentrations can be induced, shifting the doping from p^{++} to$p$.

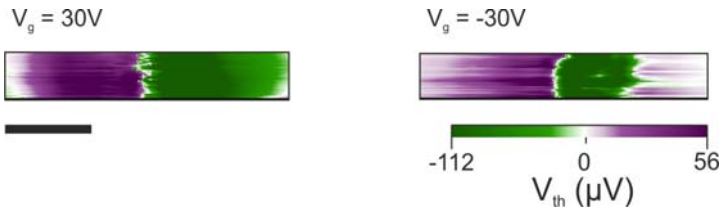

Figure S12. Gate dependent thermovoltage measurements. Global thermovoltage recorded as the hot tip is scanned over a bow tie device at two different back gate voltages $V_g = 30V$ and $V_g = -30V$.
The scale bar is 500 nm.

As can be seen in Figure S12, gating the sample does change the strength and distribution outside the constriction, however the general signal with a positive thermovoltage on the left side, a negative on the right and a node in the constriction stays the same. The change in strength and shape can be attributed to a change in the bulk Seebeck coefficient due to the varying carrier densities.[19]

13. Movement of heat by high charge carrier drift velocities

A possible mechanism of nonlinearity and cause of the asymmetry observed in the heat generation originates in the high drift velocity causing charge carriers to carry heat in a non-symmetric fashion.

For a drift velocity v_d much smaller than the Fermi velocity v_F i.e. $v_d \ll v_\mathrm{F}$, energetic hot charge carriers are dispersing from the middle of the constriction in an approximately radial pattern.

Each of the electrons carries a thermal energy of $k_B T$ and travels the mean-free-path (MFP) distance $l = \tau v_F$ on average (where τ is the relaxation time) before depositing its thermal energy within the graphene lattice, in a circle around the highest temperature spot (Figure S13 a and b).

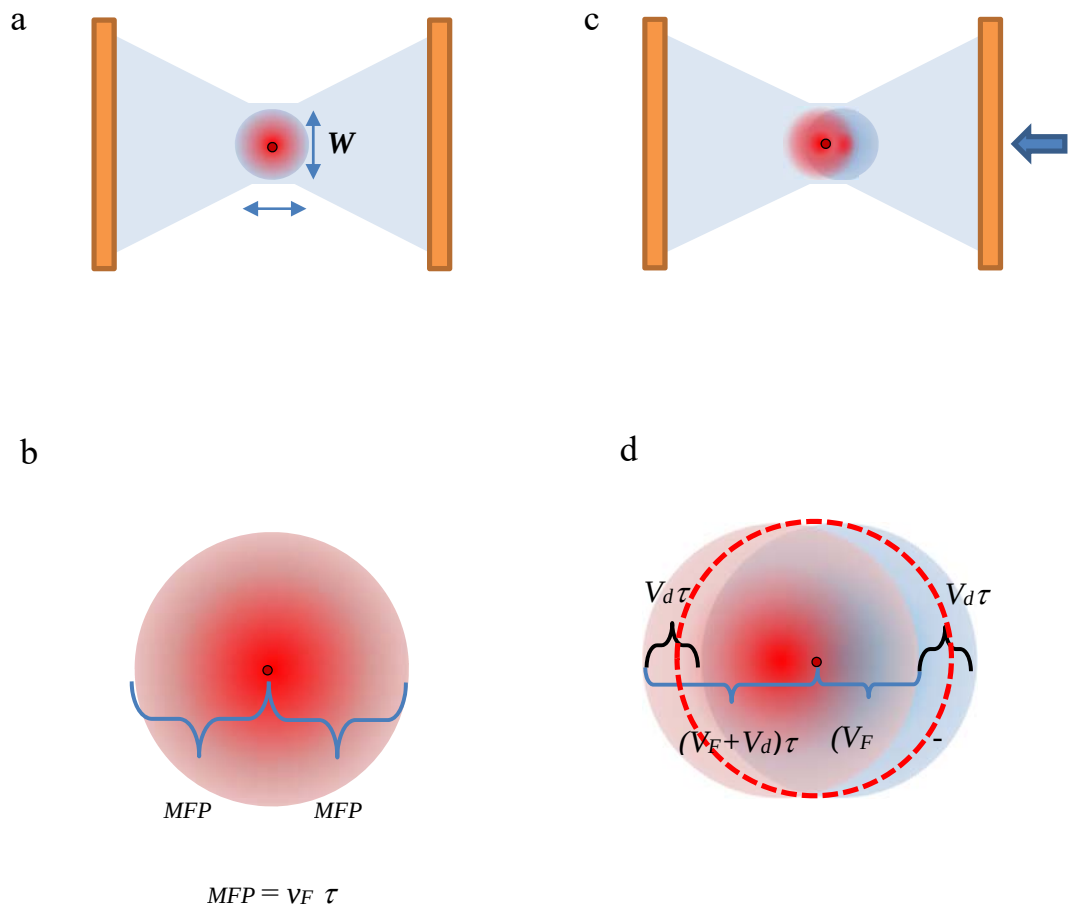

Figure S13. Illustration of the heat blowing effect due to the high drift velocity in a nanoconstriction. (a) schematic of Joule heating at low currents in a bow-tie device. (b) Schematic of Joule heating at high currents in a bow-tie device, showing the effect the shifting of the heat has. (c) Close up on the heat spot due to Joule heating at low currents in a bow-tie device. (d) Close up on the heat spot due to Joule heating at high currents in a bow-tie device, showing the effect the shifting of the heat shifting with the current direction.

In our experiments the current through the device *I* was up to 85 μA resulting in a drift velocity of $v_{\mathrm{drift}} = \frac{I}{neW} \approx 0.499 \cdot 10^6 \mathrm{ms}^{-1}$, which is on the same order as the Fermi velocity of $\approx 10^6\ \mathrm{ms}^{-1}$. As the drift velocity increases and becomes non-negligible compared to the Fermi velocity, the area where the hot electrons are depositing heat is shifted in the direction of the drift velocity by the distance $v_d\tau$ (Figure S13 c and d).

This heat produces a temperature difference along the direction of the current flow a distance $2v_F\tau$ apartIt should be noted that if the channel length *I* is much longer than $2v_d\tau$ only the entry and the exit to the channel will have this response linked to the drift velocity. This was confirmed in our measurements of graphene islands and a long ribbon, suggesting that this current drifting effect on Joule heating is most pronounced for hot spots in small constrictions.

This makes it clear, that we do not expect a linear dependence of the Peltier heating/cooling on the current in our experiment as one might conclude from $\dot{Q} = \Pi I$. Due to the strong Joule heating induced by the current, the measured signal seems to change regimes as the current is increased.

Furthermore, we tested other higher order terms in addition to a cubic dependence. As can be seen in Figure S14 4th and 5th order terms overestimate the values at lower bias while a quadratic term underestimates them. However, while the cubic fit is the best fit it should be noted that the other fits lie mostly within the

error bars and cannot be ruled out categorically.

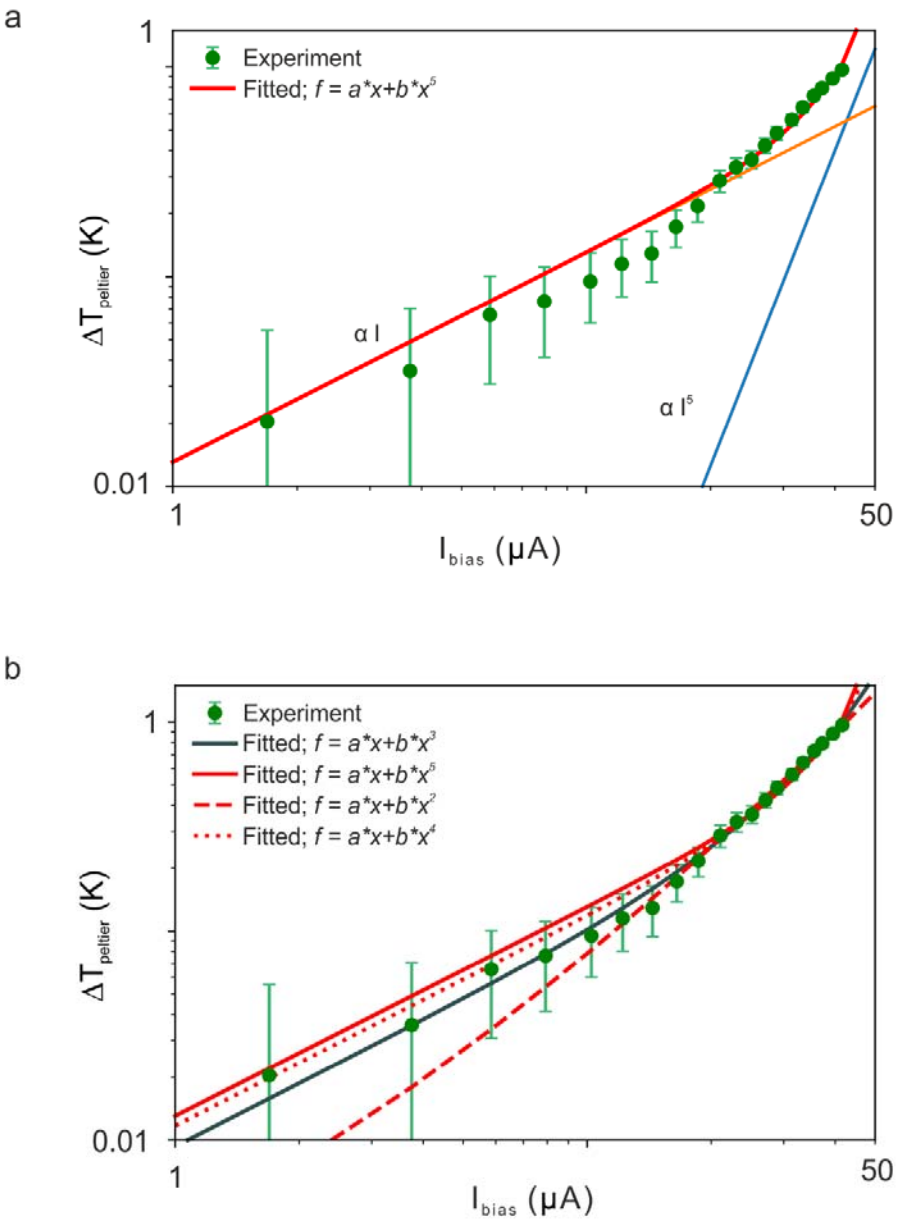

Figure S14. Different fitting parameters for the Peltier signal current dependency. (a) Linear and 5th order current dependency fit to the Peltier heating. The orange line is linear with respect to the current and the blue line is proportional to the current to the power of 5. (b) Linear and Cubic (grey), 5th order (red), quadratic (red dashed) or 4th order (red dotted) dependency of the Peltier signal on current compared to the experimental data (green dots).

14. Island geometry measurements

To test the hypothesis that a geometrical effect causing a reduction in the EMFP is responsible for the observed signal and to rule out the transport of hot/cold carriers from the Au/graphene junction at the electrodes, we investigated a "multi-island" geometry (see Figure S15). Here, wide areas alternate with constrictions, thus giving us a better control over the change from bulk to edge-scattering dominated regions and low to high current density.

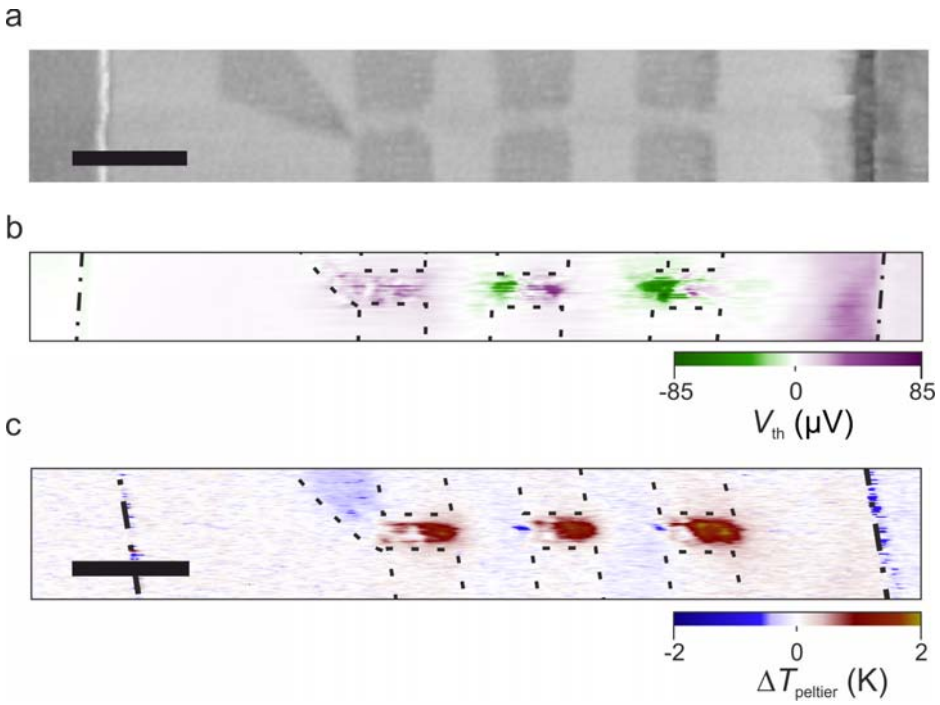

Figure S15. (a) Lateral Friction image of the island geometry. A crack in the graphene at the left side creates an additional constriction in this device. (b) Thermovoltage map of the island geometry. A pronounced signal including a sign change in the middle of each intact ribbon is visible and a fine structure in the signal can be seen that is investigated further (see SI). (c) Peltier map of the island geometry. A signal is visible within each ribbon, confirming, that the effect measured is caused by a constriction-induced change in then Seebeck coefficient. The asymmetric signal that deviates slightly from the thermovoltage signal is discussed in the main text. The scale bar is 500 nm in all figures.

As can be seen in Figure S15, the island geometry shows heating/cooling pattern and positive/negative thermovoltage at the constriction to bulk interfaces in accordance with the observed spatially dependent Seebeck coefficient due to increased edge scattering. In addition, the signal within the ribbons of reduced length shows small variations, which demonstrates the high susceptibility of the Seebeck coefficient to defects, charge puddles and small changes in width that were seen previously in photocurrent nanoscopy.[14] This sensitivity to small variations of the Seebeck coefficient inside a narrow graphene channel was further studied in long ribbons (see Figure S9), highlighting the resolution of our technique, which is able to resolve sub 20 nm features in the thermovoltage measurements.

15. Sample preparation

In order to ensure the high quality and cleanliness of the samples, they were vacuum annealed at 300 ◦C prior to measurement to remove PMMA and hydrocarbon contaminants.[20] Finally, the AFM tip was heated and quickly scanned over the sample, to completely remove remaining polymer residues naturally present on electron-beam fabricated samples prior to our measurements. The samples were at this point already loaded in the measurement SThM vacuum chamber. All devices are inherently p-doped with a charge neutrality point at 40-60V (see Figure S2), due to oxygen rich open-shell/dangling bond defects and hydrocarbon surface contamination as observed previously.[21,22]

16. Peltier signal at the contacts

In addition to the Peltier signal within the constriction, a weaker signal can be observed from the contacts that lies just above the noise level. As can be seen in Figure S16 where the Peltier signal of device 2 is shown with a saturated color scale, there are stripes or heating on the left side and stripes of cooling on the right side at the position of the contacts in addition to a slightly warmer and colder area in front of the contacts. The reason for this signal is from band bending due to doping of graphene via the metal contacts as observed previously.[23,24] Importantly, the signal from the contacts is substantially smaller than the one observed in the constriction.

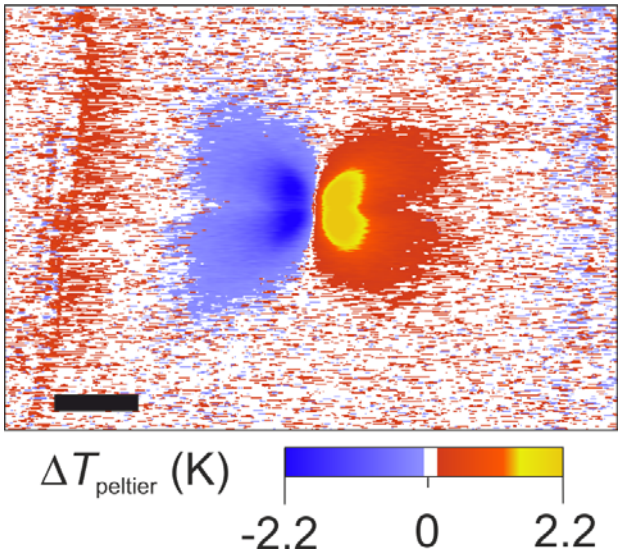

Figure S16. Saturated colorscale Peltier temperature map of device 2. While there is a rather high noise level, Peltier heating/cooling at the contacts can be observed in addition to the signal in the constriction.

References

(1) F. Menges, P. Mensch, H. Schmid, H. Riel, A. Stemmer, B. Gotsmann, *Nat. Commun.* **2016**, *7*, 10874.

(2) P. Gehring, H. Sadeghi, S. Sangtarash, C. S. Lau, J. Liu, A. Ardavan, J. H. Warner, C. J. Lambert, G. A. D. Briggs, J. A. Mol, *Nano Lett.* **2016**, *16*, 4210.

(3) Z. Y. Zhang, H. L. Xu, H. Zhong, L. M. Peng, *Appl. Phys. Lett.* **2012**, *101*, 213103

(4) Z. M. Gibbs, H.-S. Kim, H. Wang, G. J. Snyder, *Appl. Phys. Lett.* **2015**, *106*, 022112.

(5) B. Lee, K. Kim, S. Lee, J. H. Kim, D. S. Lim, O. Kwon, J. S. Lee, *Nano Lett.* **2012**, *12*, 4472.

(6) S. Gomès, A. Assy, P.-O. Chapuis, *Phys. status solidi* **2015**, *212*, 477.

(7) P. Tovee, M. Pumarol, D. Zeze, K. Kjoller, O. Kolosov, *J. Appl. Phys.* **2012**, *112*, 114317.

(8) Y. S. Muzychka, *J. Thermophys. Heat Transf.* **2014**, *28*, 313.

(9) Y. S. Muzychka, M. M. Yovanovich, J. R. Culham, *J. Thermophys. Heat Transf.* **2004**, *18*, 45.

(10) B. Gotsmann, M. A. Lantz, A. Knoll, U. Dürig, *Nanoscale Thermal and Mechanical Interactions Studies Using Heatable Probes*, Wiley-VCH Verlag GmbH & Co. KGaA, Weinheim, Germany, **2009**.

(11) F. Menges, H, Riel, A. Stemmer, C. Dimitrakopoulos, B. Gotsmann, *Phys. Rev. Lett.* **2013**, *111*, 20590.

(12) M.-H. Bae, Z. Li, Z. Aksamija, P. N. Martin, F. Xiong, Z.-Y. Ong, I. Knezevic, E. Pop *Nat. Commun.* **2013**, *4*, 1734.

(13) A. A. Balandin *Nat. Mat.* **2011**, *10*, 569

(14) A. Woessner, P. Alonso-González, M. B. Lundeberg, Y. Gao, J. E. Barrios-Vargas, G. Navickaite, Q. Ma, D. Janner, K. Watanabe, A. W. Cummings, T. Taniguchi, V. Pruneri, S. Roche, P. Jarillo-Herrero, J. Hone, R. Hillenbrand, F. H. L. Koppens, *Nat. Commun.* **2016**, *7*, 10783.

(15) E. H. Hwang, S. Adam, S. Das Sarma, *Phys. Rev. Lett.* **2007**, *98*, 186806.

(16) K. Nomura, A. H. MacDonald, *Phys. Rev. Lett.* **2007**, *98*, 076602.

(17) T. Ando, *J. Phys. Soc. Japan* **2006**, *75*, 074716.

(18) M. J. M. De Jong, *Phys. Rev. B* **1994**, *49*, 7778.

(19) Y. M. Zuev, W. Chang, P. Kim, *Phys. Rev. Lett.* **2009**, *102*, 096807.

(20) W. Xie, L.-T. Weng, K. M. Ng, C. K. Chan, C.-M. Chan, *Carbon N. Y.* **2015**, *94*, 740.

(21) S. Goniszewski, M. Adabi, O. Shaforost, S. M. Hanham, L. Hao, N. Klein, *Sci. Rep.* **2016**, *6*.

(22) R. A. Nistor, M. A. Kuroda, A. A. Maarouf, G. J. Martyna, *Phys. Rev. B* **2012**, *8622*, 41409.

(23) I. J. Vera-Marun, J. J. van den Berg, F. K. Dejene, B. J. van Wees, *Nat. Commun.* **2016**, *7*, 11525.

(24) K. L. Grosse, M.-H. Bae, F. Lian, E. Pop, W. P. King, *Nat. Nanotechnol.* **2011**, *6*, 287.